JOURNAL OF COMPUTATIONAL PHYSICS 103, 63–89 (1992)

Numerical Algorithms for Strong Discontinuities in Elastic–Plastic Solids*

JOHN A. TRANGENSTEIN AND RICHARD B. PEMBER

Computing and Mathematics Research Division, Lawrence Livermore National Laboratory L-316, P.O. Box 808, Livermore, California 94550

Received November 9, 1990; revised September 18, 1991

In this paper the implementation of second-order Godunov methods for dynamic wave propagation in one-dimensional elastic–plastic solids is investigated. First, the Lagrangian form of the algorithm is reviewed, and then the algorithm is extended to the Eulerian frame of reference. This extension requires additional evolution equations to handle the history of the material along particle paths. Both the Lagrangian and Eulerian versions of the algorithm require appropriately accurate approximations to the solution of Riemann problems, in order to represent the interaction of waves at cell boundaries. Two inexpensive approximations to the solution of the Riemann problem are constructed, and the resulting algorithms are tested against the analytic solution of the Riemann problem for longitudinal motion in an elastic–plastic bar. These approximations to the Riemann problem are shown to work well, even for strong discontinuities. Finally, the numerical experience gained from the simple longitudinal bar problem is used to design an algorithm for strong shocks predicted by a realistic soil model.

1. INTRODUCTION

The traditional approach to the numerical simulation of shocks in solids is to use piecewise linear finite elements (i.e., centered finite differences) for the spatial discretization, coupled with some form of the method of lines in time [3, 6, 33]. Typically, these methods produce significant numerical oscillations near discontinuities, unless stabilized by artificial viscosities [6, 33].

In gas dynamics, these centered-difference methods have been replaced by modern upwind shock-capturing methods, such as flux-corrected transport pioneered by Boris and Book [7] and (for example) implemented on unstructured meshes in a finite element setting by Löhner [22], total-variation diminishing techniques developed by Harten [14] and applied to aerodynamic problems by (for example) Yee [32], essentially non-oscillatory schemes developed by Harten and Osher [17] and extended by (for example) Shu [26], or higher-order Godunov methods developed by van Leer [31] and extended by (for example) Colella and Woodward [8, 10]. Our goal is to investigate the application of the last of these methods to the computation of shocks in elastic-plastic solids.

The application of upwind methods to shocks in solids has not been trivial and has required us to investigate the mathematical formulation of the problem. After writing the equations of motion in first-order form, we analyzed their characteristic structure, including the effect of rotationally invariant stress-rate measures on the acoustic tensor (cf. [23]). This enabled us to describe algorithms for the integration of one-dimensional Lagrangian equations of motion, employing an approximate Riemann solver derived from a weak-wave expansion [29].

The current stage in our research involves several new issues. One is to extend the previous Godunov method to the Eulerian frame of reference. Here, an important task is to develop additional equations to determine the evolution along particle paths of the history parameters for the plasticity models; this development is necessary because the material models are evaluated at the Eulerian cell centers, but the material particles do not stay fixed on the numerical grid in the Eulerian frame. Another difficulty with the Eulerian frame is due to the presence of unsteady contact discontinuities, such as occur at interfaces between distinct materials, or at parts of the same material with different histories. These contact discontinuities are smeared by numerical dissipation in the Eulerian front-capturing schemes since (unlike shocks) the contact discontinuities are not self-sharpening. Yet another difficulty is associated with the use of Riemann problems to determine the numerical fluxes used in the conservative difference step of Godunov's method. Ideally, these fluxes are evaluated at the stationary state in the solution to the Riemann problem. In the Lagrangian frame of reference, the flux at the stationary point is given by the flux at the constant state on either side of the contact discontinuity. In the Eulerian frame, the state

* This work was performed under the auspices of the U.S. Department of Energy by the Lawrence Livermore National Laboratory under Contract W-7405-Eng-48. Partial support was provided by the Applied Mathematical Sciences Program of the Office of Energy Research, and by the Defense Nuclear Agency.

0021-9991/92 $5.00

moving with zero speed could occur in one of the nonlinear wave families, depending on the size of the normal velocity. As a result, in the Eulerian frame it is necessary to develop more complicated approximations to the Riemann problem solution than are needed in the Lagrangian frame.

Another issue is to demonstrate the convergence of the numerical algorithms. For nonlinear solid mechanics, the existence of global solutions to initial value problems has not yet been demonstrated; furthermore, the convergence of higher-order numerical methods for hyperbolic systems has also not been established. Our approach is therefore more experimental. By using the analytic solution to the Riemann problem for the Antman–Szymczak model [30], we can test our algorithms on a set of problems that represent, in some sense, a full range of (one-dimensional) elastic–plastic waves. This set of experiments helps us to determine the applicability of our weak-wave approximation to the solution of the Riemann problem.

Our final goal in this paper is to apply the experience gained with the Antman–Szymczak model to models of practical importance. We can use the same techniques in combination with more complicated equations of state to study interesting wave propagation problems. For this example, we have selected a calculation of an explosion inside a clay sphere.

2. LONGITUDINAL MOTION IN 1D

We shall begin by describing the equations of motion for longitudinal deformation of a one-dimensional solid. Let v be the velocity, σ be the stress, ε_L be the displacement gradient, ρ_L be the density at rest, τ denote time, and x_L denote distance in the original (Lagrangian) configuration. Then conservation of momentum and equality of mixed partial derivatives of the displacement yield the following first-order system of conservation laws:

$$\frac{\partial}{\partial \tau}\begin{bmatrix} \rho_L v \\ \varepsilon_L \end{bmatrix} - \frac{\partial}{\partial x_L}\begin{bmatrix} \sigma \\ v \end{bmatrix} = 0. \tag{2.1}$$

If we allow transverse motion in the material, then the system of Eqs. (2.1) must be expanded; see [29] for details. This system of equations can be closed by prescribing a kinetic equation of state, relating the stress to other variables in the motion. However, kinetic equations of state can take a number of different forms, the description of which would take us far beyond the scope of this paper. Instead, we will describe a simple model that will be used for the bulk of our examples and introduce a more realistic model in Section 6.

In the Antman–Szymczak model [2], the stress σ is an increasing function of the displacement gradient ε_L and a history parameter π:

$$\sigma = \sigma(\varepsilon_L, \pi). \tag{2.2}$$

For any physically realistic displacement gradient ε_L, there are upper and lower bounds on the stress σ, given by the functions $c(\varepsilon_L)$ and $t(\varepsilon_L)$, representing the plastic compression and tension curves, respectively. Between these bounds, the stress is given by the elastic curves $\sigma = e(\varepsilon_L, \pi)$. Plastic compression occurs if and only if the material is at yield, and the time rate of change of the displacement gradient is negative:

$$c(\varepsilon_L) = e(\varepsilon_L, \pi) \qquad \text{and} \qquad \left.\frac{\partial \varepsilon_L}{\partial \tau}\right|_x < 0$$

during plastic compression. Similarly,

$$t(\varepsilon_L) = e(\varepsilon_L, \pi) \qquad \text{and} \qquad \left.\frac{\partial \varepsilon_L}{\partial \tau}\right|_x > 0$$

during plastic tension. There are other constraints placed on these functions and variables in order to make a consistent and realistic model; please see [2 or 30] for details. Specific forms of the elastic and plastic curves are presented at the end of the next section, where the algorithm for the evaluation of σ is described.

It is easy to see that (2.1) is hyperbolic. This is because we can write the equation in the form

$$\frac{\partial}{\partial \tau}\begin{bmatrix} \rho_L v \\ \varepsilon_L \end{bmatrix} - \begin{bmatrix} 0 & \dfrac{\partial \sigma}{\partial \varepsilon_L} \\ \dfrac{1}{\rho_L} & 0 \end{bmatrix} \frac{\partial}{\partial x_L}\begin{bmatrix} \rho_L v \\ \varepsilon_L \end{bmatrix} = 0,$$

where the eigenvectors and eigenvalues of the matrix of flux derivatives are given by

$$\begin{bmatrix} 0 & \dfrac{\partial \sigma}{\partial \varepsilon_L} \\ \dfrac{1}{\rho_L} & 0 \end{bmatrix} = \begin{bmatrix} \lambda_L \rho_L & \lambda_L \rho_L \\ -1 & 1 \end{bmatrix} \begin{bmatrix} -\lambda_L & 0 \\ 0 & \lambda_L \end{bmatrix} \begin{bmatrix} \lambda_L \rho_L & \lambda_L \\ -1 & 1 \end{bmatrix}^{-1}.$$

Since stress is an increasing function of the displacement gradient, the characteristic speed

$$\lambda_L = \sqrt{(1/\rho_L)(\partial \sigma / \partial \varepsilon_L)} \tag{2.3}$$

is real. For material particles at the elastic limit, this characteristic speed is not uniquely defined; depending on the loading direction, the appropriate characteristic speed may be given by the slope of the elastic curves during unloading, or by the slope of the appropriate plastic curve during plastic yield.

We also note that the total energy density

$$v = \tfrac{1}{2}\rho_L \mathbf{v}^2 + \int_{\varepsilon_0}^{\varepsilon_L} \sigma \, d\varepsilon_L,$$

is the "entropy function" for (2.1) [12]; the "entropy flux" is the rate of work per volume

$$\phi = -\mathbf{v}\sigma.$$

Since v is a convex entropy function, we can add a small viscous term to the right-hand side of (2.1) and derive

$$\frac{\partial v}{\partial \tau} + \frac{\partial \phi}{\partial x} \leqslant 0,$$

in the limit as the viscosity approaches zero [21]. This shows that for motions achieved in the limit of vanishing viscosity, the total energy cannot increase in time.

We also note that at a discontinuity, the solution to (2.1) satisfies the jump conditions [11]

$$-\begin{bmatrix} 0 \\ \sigma \\ \mathbf{v} \end{bmatrix}_R + \begin{bmatrix} 0 \\ \sigma \\ \mathbf{v} \end{bmatrix}_L = \left\{ \begin{bmatrix} \rho_L \\ \rho_L \mathbf{v} \\ \varepsilon_L \end{bmatrix}_R - \begin{bmatrix} \rho_L \\ \rho_L \mathbf{v} \\ \varepsilon_L \end{bmatrix}_L \right\} s, \quad (2.4)$$

where the subscripts on the square brackets label the states on the two sides of the discontinuity, and s is the speed of the discontinuity. Thus, at a zero-speed discontinuity (i.e., a contact discontinuity), the velocity and stress are continuous while the density, strain and displacement may have jumps. At a moving discontinuity the density is continuous while the velocity, stress, strain, and displacement may jump. In this case, we can write the shock speed in the form

$$s = \pm\sqrt{(1/\rho_L)(\sigma_R - \sigma_L)/((\varepsilon_L)_R - (\varepsilon_L)_L)}.$$

At a discontinuity achieved in the limit of vanishing viscosity, the entropy function satisfies

$$(\phi_R - \phi_L) \leqslant (v_R - v_L)s.$$

Since the entropy function is convex, it is also possible to show [12] that the chord condition

$$0 \leqslant s\left\{\frac{\sigma_* - \sigma_L}{\varepsilon_* - (\varepsilon_L)_L} - \frac{\sigma_R - \sigma_L}{(\varepsilon_L)_R - (\varepsilon_L)_L}\right\} \quad (2.5)$$

must be satisfied for all ε_* between $(\varepsilon_L)_L$ and $(\varepsilon_L)_R$.

Next, we will describe the Eulerian form of the equations of motion,

$$\frac{\partial u}{\partial \tau} + \frac{\partial f}{\partial x_E} = 0. \quad (2.6)$$

Here the vectors of conserved quantities and fluxes are (respectively)

$$u = \begin{bmatrix} \rho_E \\ \rho_E \mathbf{v} \\ \varepsilon_E \\ \rho_E \pi_0 \end{bmatrix}, \qquad f = \begin{bmatrix} \rho_E \mathbf{v} \\ \rho_E \mathbf{v}^2 - \sigma \\ \mathbf{v}(1+\varepsilon_E) \\ \rho_E \pi_0 \mathbf{v} \end{bmatrix}.$$

Also, $\rho_E = \rho_L(1+\varepsilon_L)$ is the density in the current configuration,

$$\varepsilon_E = -\frac{\varepsilon_L}{1+\varepsilon_L}$$

is the Eulerian displacement gradient, π_0 is the plastic history parameter at the beginning of the particle path that leads to the current particle position, and x_E is position in the current configuration.

3. LAGRANGIAN ALGORITHM

At this point we have described the problem in both the Lagrangian and Eulerian frames of reference, discussed the hyperbolicity and characteristic speeds for the equations of motion, and presented the conditions determining physically correct shocks. The next task is to describe our approach to the numerical solution. We will begin with the Lagrangian version of the method. There are six steps in our second-order algorithm:

1. characteristic analysis and timestep estimation,
2. monotonized slope computation,
3. characteristic tracing,
4. flux computation,
5. conservative differences, and
6. stress update.

We begin a timestep with cell-centered values of the velocities, displacement gradients and stresses. Our goal is to compute these quantities at the next time level.

The first step requires that we compute characteristic speeds associated with the current loading conditions; this is discussed in detail in [29]. In particular, the characteristic speeds and directions can be determined from the eigenvalues and eigenvectors of the acoustic tensor. For the Antman–Szymczak model, the form of the characteristic speed was derived in (2.3). As we noted above, this speed is not uniquely defined when the material is at an elastic limit. For example, in cells undergoing plastic compression at the beginning of the timestep we take $\lambda_L = \sqrt{(1/\rho_L)(\partial c/\partial \varepsilon_L)}$. For plastic tension, we take $\lambda_L = \sqrt{(1/\rho_L)(\partial t/\partial \varepsilon_L)}$. Otherwise, we use the elastic speed, $\lambda_L = \sqrt{(1/\rho_L)/(\partial e/\partial \varepsilon_L)}$. However, for purposes of determining the size of the timestep, we always use the fastest *elastic* speed in a

Courant–Friedrichs–Lewy (CFL) condition and typically reduce it by some factor (called the CFL factor) to allow for the discrete sampling of the larger characteristic speeds that may form during the motion. This timestep selection uses the elastic speed because it is always larger than the plastic speeds, and the timestep must be limited by the fastest characteristic speed that might occur in the motion.

The next step in the algorithm is to compute the monotonized slopes. The goal of this step is to construct values for the flux variables (i.e., σ and $\mathbf{v}$) at the cell edges. Here, we remark that two alternatives are possible. We could have applied the Godunov algorithm in the traditional form, by constructing slopes in the conserved quantities $\rho\mathbf{v}$ and ε, as in [2]. One drawback of this approach is that it introduces numerical viscosity at contact discontinuities, where velocity and stress are continuous but displacements and their gradients can be discontinuous. Another disadvantage of the traditional approach to the Godunov method is that it is necessary to call the equation of state at each side of the cell edge to compute fluxes in the solution of the Riemann problem. (That is, stress must be computed from the traced displacement gradients.) This leads to additional computational expense; in fact, for complicated equations of state, the determination of stress is the dominant cost. On the other hand, one possible difficulty with our approach is that the stresses we construct at the cell edges are not realizations of the equation of state and may therefore by "unphysical," meaning that they could violate constraints such as yield conditions.

Let us describe our approach to the slope construction. First, we rewrite the equations of motion in the quasilinear form (cf. [19])

$$\frac{\partial}{\partial\tau}\begin{bmatrix}\mathbf{v}\\ \sigma\end{bmatrix}-\begin{bmatrix}0 & \dfrac{1}{\rho_L}\\ \dfrac{\partial\sigma}{\partial\varepsilon_L} & 0\end{bmatrix}\frac{\partial}{\partial x_L}\begin{bmatrix}\mathbf{v}\\ \sigma\end{bmatrix}=0. \tag{3.1}$$

Note that the second equation in (3.1) is derived from the equation of state (2.2) by differentiating it in time and using the second equation in (2.1). In the particular case of the Antman–Szymczak model, no terms involving $\partial\pi/\partial\tau$ appear in the linearization for two reasons: in elastic response, the plastic history π is constant, and in plastic response, the stress σ is independent of π. Also note that the linearized coefficient matrix has a characteristic structure given by

$$\begin{bmatrix}0 & \dfrac{1}{\rho_L}\\ \dfrac{\partial\sigma}{\partial\varepsilon_L} & 0\end{bmatrix}=\begin{bmatrix}1 & -1\\ \lambda_L\rho_L & \lambda_L\rho_L\end{bmatrix}\begin{bmatrix}-\lambda_L & 0\\ 0 & \lambda_L\end{bmatrix}\begin{bmatrix}1 & -1\\ \lambda_L\rho_L & \lambda_L\rho_L\end{bmatrix}^{-1}.$$

These results allow us to expand the jumps in cell averages of the flux variables in terms of eigenvectors of the linearized coefficient matrix:

$$\begin{bmatrix}\Delta\mathbf{v}\\ \Delta\sigma\end{bmatrix}^k_{j+1/2}=\begin{bmatrix}\mathbf{v}\\ \sigma\end{bmatrix}^k_{j+1}-\begin{bmatrix}\mathbf{v}\\ \sigma\end{bmatrix}^k_j,$$

$$\begin{bmatrix}\Delta c^-\\ \Delta c^+\end{bmatrix}_{j,\mathrm{R}}=\begin{bmatrix}1 & -1\\ (\lambda\rho)^k_j & (\lambda\rho)^k_j\end{bmatrix}^{-1}\begin{bmatrix}\Delta\mathbf{v}\\ \Delta\sigma\end{bmatrix}^k_{j+1/2}=\begin{bmatrix}\Delta\sigma^k_{j+1/2}/(\lambda\rho)^k_j+\Delta\mathbf{v}^k_{j+1/2}\\ \Delta\sigma^k_{j+1/2}/(\lambda\rho)^k_j-\Delta\mathbf{v}^k_{j+1/2}\end{bmatrix},$$

$$\begin{bmatrix}\Delta c^-\\ \Delta c^+\end{bmatrix}_{j,\mathrm{L}}=\begin{bmatrix}1 & -1\\ (\lambda\rho)^k_j & (\lambda\rho)^k_j\end{bmatrix}^{-1}\begin{bmatrix}\Delta\mathbf{v}\\ \Delta\sigma\end{bmatrix}^k_{j+1/2}=\begin{bmatrix}\Delta\sigma^k_{j-1/2}/(\lambda\rho)^k_j+\Delta\mathbf{v}^k_{j-1/2}\\ \Delta\sigma^k_{j-1/2}/(\lambda\rho)^k_j-\Delta\mathbf{v}^k_{j-1/2}\end{bmatrix},$$

$$\begin{bmatrix}\Delta c^-\\ \Delta c^+\end{bmatrix}_{j,C}=\left(\begin{bmatrix}\Delta c^-\\ \Delta c^+\end{bmatrix}_{j,\mathrm{R}}+\begin{bmatrix}\Delta c^-\\ \Delta c^+\end{bmatrix}_{j,\mathrm{L}}\right)\frac{1}{2}.$$

Afterward, the expansion coefficients $\Delta c^\pm$ are adjusted to prevent the introduction of new extrema [8]:

$$\Delta c^\pm=\min\{|(\Delta c^\pm)_\mathrm{L}|,|(\Delta c^\pm)_\mathrm{R}|,\tfrac{1}{2}|(\Delta c^\pm)_C|\}\times\{\operatorname{sign}\{(\Delta c^\pm)_\mathrm{L}\}+\operatorname{sign}\{(\Delta c^\pm)_\mathrm{R}\}\}.$$

This step is analogous to a local decoupling of the equations of motion into a set of scalar evolution equations, and the slope limiting procedure has the effect of introducing a selective numerical viscosity in individual wave families [27]. Note that the contribution of the numerical viscosity to the momentum equation is analogous to the introduction of a viscous force, and the contribution to the stress-rate equation is analogous to the introduction of a visco-elastic term in the constitutive law.

Recall that the characteristic speeds change discontinuously from elastic to plastic behavior. This discontinuity destroys the ability of the slope construction to obtain second-order accuracy and may require the numerical scheme to separate an initial discontinuity into two distinct shocks traveling in the same direction with different speeds. As a result, at all cell edges where the neighboring cells are undergoing different loading conditions we set the slopes to zero; that is, we fall back to the first-order Godunov method.

We also note two other possible situations under which the slopes undergo further modification. In the Eulerian version of the algorithm, we use fourth-order slopes to improve the resolution of contact discontinuities; this is discussed further in the next section. For strong sharp discontinuities it is useful to introduce additional slope limiting to reduce numerical oscillations; this slope flattening process is described in Section 5.

Our next step is to use the limited slopes in the characteristic families to construct values for the flux variables at the left- and right-hand sides of the cell edges at the half-time level. This is accomplished by performing a Taylor expansion about the cell centers in order to approximate the values at the cell edges and half-time levels, using the quasilinear form (3.1) to replace the time derivative in the Taylor expansion, and multiplying by the left eigenvectors of A to find the characteristic quantities, and then throwing away characteristic information that goes the wrong way:

$$\begin{bmatrix} \mathbf{v} \\ \sigma \end{bmatrix}^{k+1/2}_{j+1/2,\mathrm{L}} = \begin{bmatrix} \mathbf{v} \\ \sigma \end{bmatrix}^{k}_{j} + \begin{bmatrix} -1 \\ \lambda_L \rho_L \end{bmatrix}^{k}_{j} \frac{1}{2}\left\{1 - (\lambda_L)^k_j \frac{\Delta}{\Delta x_L}\right\} \Delta c^+_j,$$

$$\begin{bmatrix} \mathbf{v} \\ \sigma \end{bmatrix}^{k+1/2}_{j+1/2,\mathrm{R}} = \begin{bmatrix} \mathbf{v} \\ \sigma \end{bmatrix}^{k}_{j+1} - \begin{bmatrix} 1 \\ \lambda_L \rho_L \end{bmatrix}^{k}_{j+1} \frac{1}{2}\left\{1 - (\lambda_L)^k_{j+1} \frac{\Delta\tau}{\Delta x_L}\right\} \Delta c^-_{j+1}.$$

We note that an alternative approach is to limit slopes in $\mathbf{v}$ and σ directly, then compute the expansion coefficients of the limited slopes and continue the characteristic tracing.

Afterward, we resolve the interaction of the waves between the left and right states through the approximate solution of a Riemann problem. Note that there are good reasons for developing an approximate Riemann solver. Although an analytic Riemann solver is available for the Antman–Szymczak model, it is far too expensive to use in practice. The more serious problem is that for general equations of state, the analytic solution of the Riemann problem is unknown. Thus our approach is to develop an approximate Riemann solver by testing it on a problem for which the solution is known.

In developing an approximate Riemann solver, we have several goals in mind. The first is that the Riemann solver must be second-order accurate for weak waves. This is in contrast to the approach in Antman and Szymczak [2], where an approximate Riemann solver is employed, using only bounds on the characteristic speeds. For systems of two equations, our approach is more similar to that of Harten *et al.* [16], where an approximate Riemann solver employing one intermediate state is developed. However, their approximate Riemann solver views the Godunov method in terms of averaging an approximate evolution operator instead of formulating a conservative difference. A consequence of this formulation is that their method would introduce numerical viscosity at all jumps in the displacement gradient, even contact discontinuities. This violates our second principle, that we avoid the addition of numerical viscosity at contact discontinuities in the Lagrangian frame.

Our third design principle is that the Riemann solver must be extendible to a second-order scheme for more general deformations involving shear, in which there may be as many as six nonzero characteristic speeds, plus a zero speed for the contact discontinuities, and therefore six intermediate states. If we viewed the Godunov method in terms of averaging the evolution of the Riemann problem solution, as in [16], instead of constructing a conservative difference approximation, then the treatment of six intermediate states would be difficult. Another design goal is to enforce some form of an entropy condition for strong waves. In this regard, we note that one of the attractions of the approach in [16] is that the approximate Riemann solver can be shown to satisfy an entropy condition. However, the proof requires that an entropy function exist, which is not true for many of the applied models for solids (many of the hypoelastic models do not even possess a strain energy [4]). Our alternative approach will be to adjust the numerical diffusion in the approximate solution to the Riemann problem, taking care that sufficient diffusion is introduced near strong discontinuities (see Section 5).

In this section, we will describe an approximate Riemann solver that satisfies the first three of our design goals; this scheme will be modified in Section 5 to handle strong discontinuities. The starting point in the approximate Riemann solver is to use the available characteristic information to construct an approximate path in flux-variable space for the wave interaction. First, we decompose the jump in terms of the characteristic directions, by computing the expansion coefficients $a^{\pm}$:

$$\begin{bmatrix} a^- \\ a^+ \end{bmatrix} = \begin{bmatrix} 1 & -1 \\ (\lambda_L\rho_L)^k_j & (\lambda_L\rho_L)^k_{j+1} \end{bmatrix}^{-1} \left\{ \begin{bmatrix} \mathbf{v} \\ \sigma \end{bmatrix}^{k+1/2}_{j+1/2,\mathrm{R}} - \begin{bmatrix} \mathbf{v} \\ \sigma \end{bmatrix}^{k+1/2}_{j+1/2,\mathrm{L}} \right\}.$$

Next, we approximate the state that remains stationary, by either of two equivalent expressions:

$$\begin{bmatrix} \mathbf{v} \\ \sigma \end{bmatrix}^{k+1/2}_{j+1/2} = \begin{bmatrix} \mathbf{v} \\ \sigma \end{bmatrix}^{k+1/2}_{j+1/2,\mathrm{L}} + \begin{bmatrix} 1 \\ \lambda_L\rho_L \end{bmatrix}^{k}_{j} a^- = \begin{bmatrix} \mathbf{v} \\ \sigma \end{bmatrix}^{k+1/2}_{j+1/2,\mathrm{R}} - \begin{bmatrix} -1 \\ \lambda_L\rho_L \end{bmatrix}^{k}_{j+1} a^+.$$

This approximate Riemann solver is very simple to implement and works well for weak waves. Note that we have previously used this Riemann solver in one-dimensional problems involving both longitudinal and transverse motion. Even in this complicated setting, the algorithm reduces to the solution of at most a 3×3 system of equations [29].

In the next step of the Godunov method, we update the

conserved quantities, namely momentum and displacement gradient, using the following finite difference calculation derived from (2.1) and the divergence theorem:

$$\begin{bmatrix} \mathbf{v}\rho_L \\ \varepsilon_L \end{bmatrix}_j^{k+1} = \begin{bmatrix} \mathbf{v}\rho_L \\ \varepsilon_L \end{bmatrix}_j^{k} + \frac{\Delta\tau}{\Delta x_L} \left\{ \begin{bmatrix} \sigma \\ \mathbf{v} \end{bmatrix}_{j+1/2}^{k+1/2} - \begin{bmatrix} \sigma \\ \mathbf{v} \end{bmatrix}_{j-1/2}^{k+1/2} \right\}.$$

Note that our difference scheme conserves momentum exactly. Furthermore, discrete traveling discontinuities satisfy equations that are discrete forms of the Rankine–Hugoniot conditions (2.4). The difference equations for the displacement gradient can also be derived from the equation for the displacements at the cell edges,

$$d_{j+1/2}^{k+1} = d_{j+1/2}^{k} + \mathbf{v}_{j+1/2}^{k+1/2}\,\Delta\tau,$$

$$(\varepsilon_L)_j^{k+1} = \frac{d_{j+1/2}^{k+1} - d_{j-1/2}^{k+1}}{\Delta x_L}.$$

In other words, for one-dimensional computations it is equivalent to compute the cell-centered values of the displacement gradient as spatial gradients of the displacement. At the end of this step, we have updated the velocity and displacement gradient to the new time level.

All that remains is to update the stresses and history parameters. This step depends on the model being used. For simple problems, such as the Antman–Szymczak model, the stress update is very inexpensive. The process begins with the old value of the history parameter π and the new value of the displacement gradient ε_L. Then we perform the following computations:

$$\sigma := \max\{c(\varepsilon_L), \min\{e(\varepsilon_L, \pi), t(\varepsilon_L)\}\};$$

$$\text{if } \sigma = c(\varepsilon_L) \text{ solve } \sigma = e(\varepsilon_L, \pi) \text{ for } \pi,$$

$$\text{elseif } \sigma = t(\varepsilon_L) \text{ solve } \sigma = e(\varepsilon_L, \pi) \text{ for } \pi.$$

This produces new values for the stress σ and the history parameter π. For other models, such as hypoelastic models, the stress update is significantly more complicated, involving the determination of strain rates, rotation to an indifferent frame of reference, and the integration of constrained ordinary differential equations. In order to maintain the overall accuracy of the Godunov method, it is necessary that these computations be second-order accurate. An example of the application of second-order Godunov methods to a hypoelastic model, and of the modifications to the algorithm for the equation of state, can be found in [28].

As numerical examples, we present the results of two computations using the Godunov method presented above, in combination with the Antman–Szymczak model. Here, we have chosen the model functions to be

$$e(\varepsilon_L, \pi) = -\frac{0.49}{0.7 + \varepsilon_L - \pi} + 0.7 + \varepsilon_L - \pi,$$

$$c(\varepsilon_L) = -0.1 - \frac{1}{(1+\varepsilon_L)^2},$$

$$t(\varepsilon_L) = 1.1 - \frac{1}{\sqrt{2+\varepsilon_L}}.$$

The first of our examples represents the typical case in impact problems, where an elastic precursor and a plastic shock travel away from the point of impact. In this case, the initial discontinuity is at the center of the grid, with $\pi = 0.93$, $\varepsilon_L = 1.161$, and $\mathbf{v} = 0$ in the left-hand material, and $\pi = 0.35$, $\sigma = -0.252$, and $\mathbf{v} = -1.081$ in the right-hand material. The second of our examples has been chosen because it is particularly difficult for the Eulerian version of the algorithm, as we will see in the next section. In this example there is a weak elastic shock, a substantial contact discontinuity, and elastic and plastic rarefactions. Again, the initial discontinuity is at the center of the grid, with $\pi = 4$, $\varepsilon_L = 4.397$, and $\mathbf{v} = 0$ in the left-hand material, and $\pi = 0.3$, $\sigma = -0.05$, and $\mathbf{v} = 0.468$ in the right-hand material.

The numerical results for these two calculations, computed with a CFL factor of 0.9, are shown in Figs. 1 and 2. In the upper left-hand plot of each figure, the path chosen by the solution of the Riemann problem is shown in velocity-stress space, while the stress-strain relationship is shown in the top right-hand plot. Since the solution of a Riemann problem is self-similar, we plot velocity, stress, displacement gradient, and characteristic speed versus the similarity variable, namely, distance from the initial discontinuity divided by elapsed time. Thus the horizontal axis of these figures can be used to read the shock speeds, and the plot of the Lagrangian characteristic speed versus the similarity variable can be used to verify the satisfaction of the Lax entropy condition [20]. The solid lines represent fine grid calculations with 1000 cells; the plus signs represent the results of the same calculation with 100 cells. Note that shocks are typically resolved in two to three cells, and rarefactions are accurately resolved. Also note that the plots of characteristic speeds may show some significant variations in the middle of constant states on a yield surface; these are due to the two choices of characteristic speed available to the algorithm. Tiny numerical oscillations will cause the algorithm to switch from plastic loading to elastic unloading or vice versa.

4. EULERIAN ALGORITHM

The Lagrangian and Eulerian frames of reference each have advantages and disadvantages for simulation. Com-

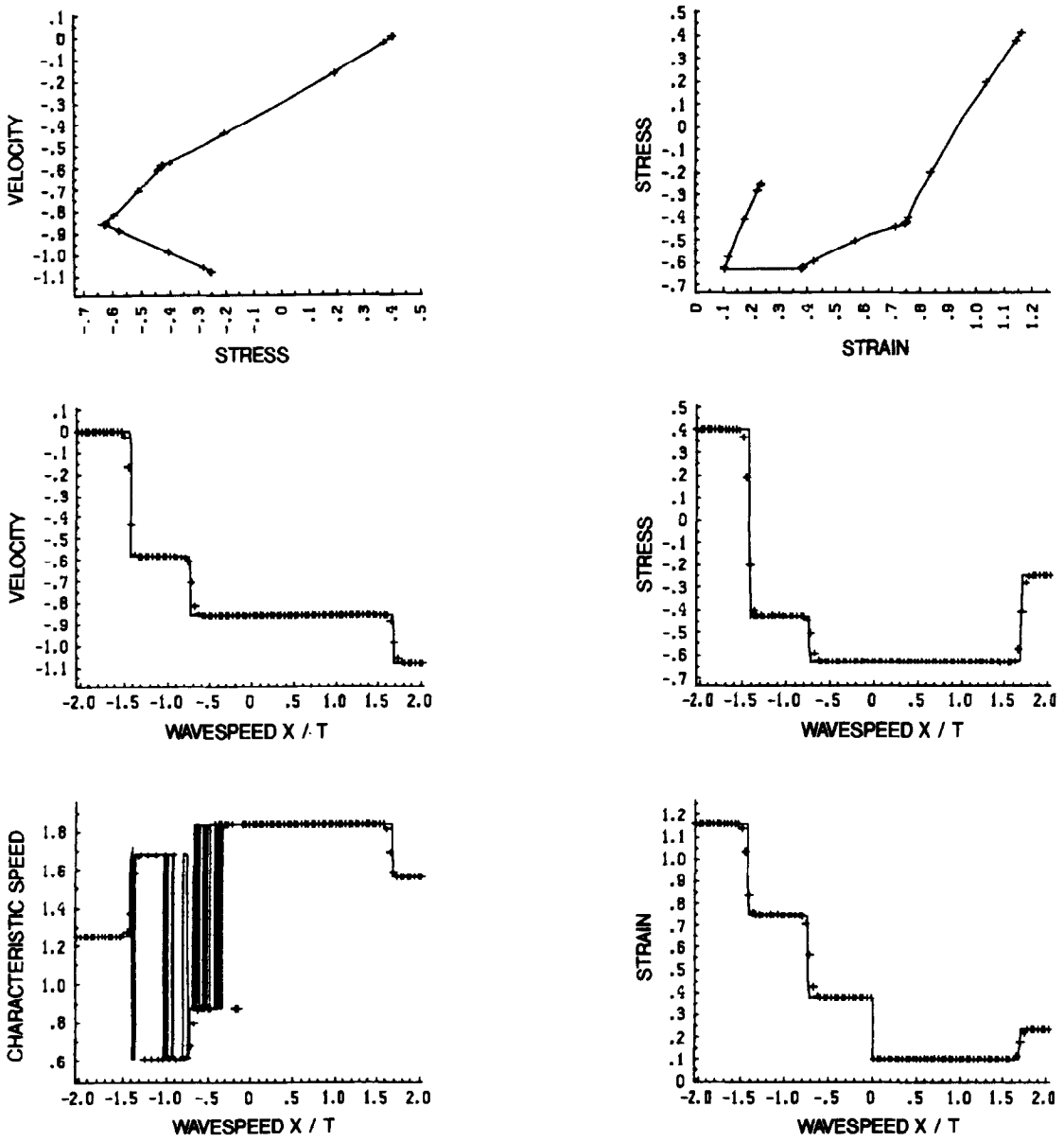

FIG. 1. Lagrangian calculation with elastic precursor and plastic shock.

putations in the Lagrangian frame of reference are useful for keeping material interfaces separate, since the material interfaces are tracked by the computation. However, Lagrangian calculations can require smaller timesteps near strong discontinuities. Furthermore, the Lagrangian calculations can fail near strong rotations. For updated Lagrangian calculations (in which the grid moves with the material particles), cell inversions or multi-dimensional bow-ties can occur; for true Lagrangian calculations, the determinant of the deformation gradient can become zero or negative. On the other hand, Eulerian calculations are useful for strong rotations (e.g., shear bands and cratering), since the grid cells (typically) stay fixed in the current frame of reference. However, Eulerian calculations typically smear contact discontinuities. Furthermore, Eulerian calculations for solids are more expensive: they involve the solution of a larger system of equations, and the solution of the Riemann problem is more difficult to approximate.

In this section, we will describe an Eulerian version of the higher-order Godunov method. One purpose of this work is to develop the techniques required to approximate the solution of the Riemann problems. However, if we are willing to put the problem in a frame of reference moving sufficiently fast (i.e., faster than the characteristic speeds of the material) then the solution of the Riemann problems is trivial, since it is given by the upwind state.

This observation allows us to run calculations using an exact Riemann problem solution no matter what the model might be and to compare the results against calculations requiring approximate Riemann problem solutions (such as Lagrangian calculations).

Let us begin the description of the Eulerian algorithm. Note that the flux vector f in the Eulerian form of the equations of motion (2.6) is a function of the flux variables unlike the Lagrangian case, the vector of Eulerian flux variables is larger than the vector of conserved quantities. As before, we can determine a quasilinear form (3.1) for the flux variables, obtaining the linearized coefficient matrix

$$w = \begin{bmatrix} \rho_E \\ \mathrm{v} \\ \sigma \\ \varepsilon_E \\ \pi_0 \end{bmatrix};$$

$$A = \begin{bmatrix} \mathrm{v} & \rho_E & 0 & 0 & 0 \\ 0 & \mathrm{v} & -\dfrac{1}{\rho_E} & 0 & 0 \\ 0 & \dfrac{\partial \sigma}{\partial \varepsilon_E}(1+\varepsilon_E) & \mathrm{v} & 0 & 0 \\ 0 & 1+\varepsilon_E & 0 & \mathrm{v} & 0 \\ 0 & 0 & 0 & 0 & \mathrm{v} \end{bmatrix},$$

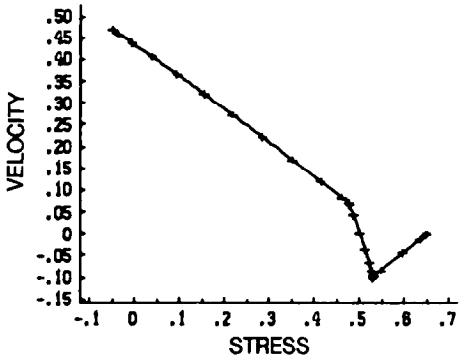

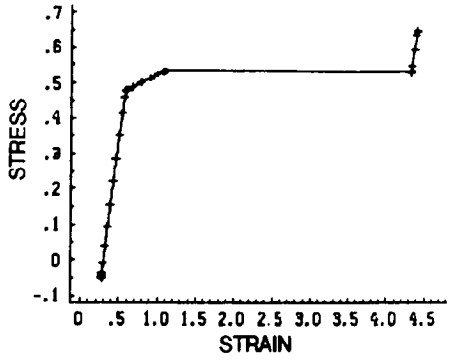

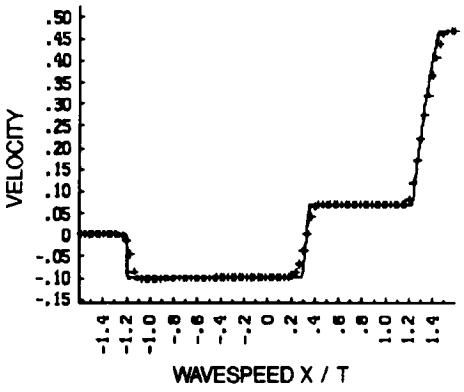

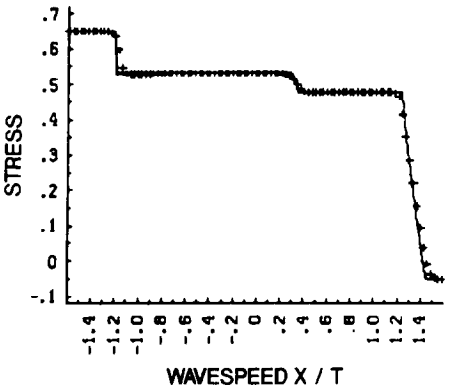

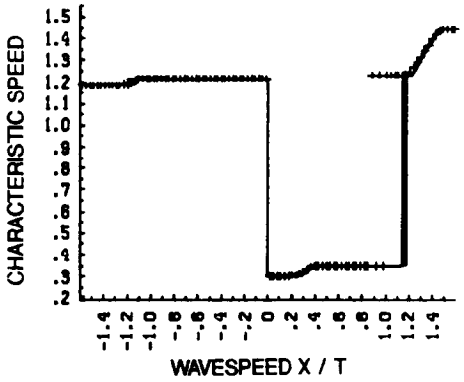

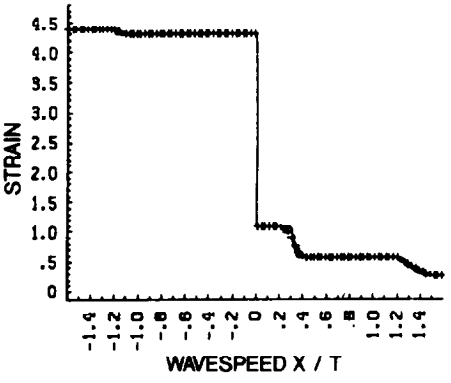

FIG. 2. Lagrangian calculation with elastic and plastic rarefactions.

for which the matrix of eigenvectors is

$$X=\begin{bmatrix} -\rho_E & 1 & 0 & 0 & -\rho_E \\ \lambda_E & 0 & 0 & 0 & -\lambda_E \\ \lambda_E^2\rho_E & 0 & 0 & 0 & \lambda_E^2\rho_E \\ -1-\varepsilon_E & 0 & 1 & 0 & -1-\varepsilon_E \\ 0 & 0 & 0 & 1 & 0 \end{bmatrix},$$

and the matrix of eigenvalues is

$$\Lambda=\begin{bmatrix} \mathbf{v}-\lambda_E & 0 & 0 & 0 & 0 \\ 0 & \mathbf{v} & 0 & 0 & 0 \\ 0 & 0 & \mathbf{v} & 0 & 0 \\ 0 & 0 & 0 & \mathbf{v} & 0 \\ 0 & 0 & 0 & 0 & \mathbf{v}+\lambda_E \end{bmatrix}.$$

Here, the eulerian characteristic speed is

$$\lambda_E^2=-\frac{\partial\sigma}{\partial\varepsilon_E}\frac{1+\varepsilon_E}{\rho_E}=\frac{\partial\sigma}{\partial\varepsilon_L}\frac{1}{\rho_L}\frac{1}{(1+\varepsilon_E)^2}=\left(\frac{\lambda_L}{1+\varepsilon_E}\right)^2.$$

Most of the steps in the Eulerian higher-order Godunov method now carry over as in the Lagrangian case. The absolute value of the largest characteristic speed is $\lambda_E+|\mathbf{v}|$, and the timestep is chosen using the elastic values for λ_E. The monotonized slope construction is similar to the Lagrangian case as well. In other words, we compute expansion coefficients

$$\Delta c=X^{-1}\,\Delta w=\begin{bmatrix} \left(\Delta\mathbf{v}+\dfrac{\Delta\sigma}{\rho_E\lambda_E}\right)\Big/(2\lambda_E) \\ \Delta\rho_E+\Delta\sigma/\lambda_E^2 \\ \Delta\varepsilon_E+\Delta\sigma(1+\varepsilon_E)/\rho_E\lambda_E^2 \\ \Delta\pi_0 \\ \left(-\Delta\mathbf{v}+\dfrac{\Delta\sigma}{\rho_E\lambda_E}\right)\Big/(2\lambda_E) \end{bmatrix}$$

and limit these in the usual fashion.

We use fourth-order slopes to steepen the contact discontinuities. These are computed simply by Richardson extrapolation of centered differences at distances of two cells and four cells apart. Although subcell resolution [15] would have given much better resolution of the contacts, we did not use this approach because it has not yet been generalized to multiple spatial dimensions. On the other hand, second- and fourth-order slopes can be determined in individual coordinate directions and then used in an unsplit multi-dimensional version of Godunov's method [9].

In the characteristic tracing step, the Taylor expansion, replacement of the time derivative by the quasilinear form, and eigenvector replacement proceed as in the Lagrangian case. All that is left is the characteristic projection. The left states at cell edges and half-time levels are built up as a sum over positive eigenvalues of the linearized coefficient matrix, and the right states sum over negative eigenvalues:

$$w_{j+1/2,\mathrm{L}}^{k+1/2}=w_j^k+\sum_{\lambda_i>0}X_j^k e_i\frac{1}{2}\left\{1-(\lambda_i)_j^k\frac{\Delta\tau}{\Delta x_E}\right\}\Delta c_i,$$

$$w_{j-1/2,\mathrm{R}}^{k+1/2}=w_j^k-\sum_{\lambda_i<0}X_j^k e_j\frac{1}{2}\left\{1+(\lambda_i)_{j+1}^k\frac{\Delta\tau}{\Delta x_E}\right\}\Delta c_i.$$

Here e_i is the ith axis vector in the Euclidean space of appropriate dimension.

Unlike the previous steps, the approximate solution of the Riemann problem is significantly more complicated in the Eulerian frame than in the Lagrangian frame. The essential ideas for our approximate Riemann solver are contained in Bell *et al.* [5], which was inspired by the work of Engquist and Osher [13].

Because we use the divergence theorem to derive the conservative difference equations, the evaluation of the time integral of the flux at a cell edge requires an approximation to the flux at the stationary state in the Riemann problem. In the Lagrangian frame of reference, this is relatively easy to find, because the waves exhibit reflection symmetry (i.e., the characteristic speeds come in plus/minus pairs); as a result, the stationary state must be the constant state between the left-moving and right-moving waves. Actually, this constant state may be split at zero speed by a contact discontinuity, but the Rankine–Hugoniot conditions for this contact discontinuity show that the flux must be continuous across the Lagrangian contact. In this case, we merely average the fluxes on either side [29]. In the Eulerian frame, the stationary state in the solution of the Riemann problem might occur in the middle of one of the nonlinear waves; this requires extra care.

First, we decompose the jump between the left and right states in terms of the expansion eigenvectors, which are chosen as in the Lagrangian frame (eigenvectors with eigenvalues $\mathbf{v}-\lambda_E$ chosen from the left cell, eigenvectors with eigenvalues $\mathbf{v}+\lambda_E$ chosen from the right, and the other eigenvectors are constant):

$$w_{j+1/2,\mathrm{R}}^{k+1/2}-w_{j+1/2,\mathrm{L}}^{k+1/2}=X_j^k e_1 a_1+\sum_{i=2}^{4}Xe_i a_i+X_{j+1}^k e_5 a_5.$$

Next, we check for transonic waves (waves with a change in the sign of the characteristic speeds) and determine whether the reference state for the Engquist–Osher flux should be the left or the right. Our principal objective is to avoid, as much as possible, an Engquist–Osher flux approximation involving the linearly degenerate waves (those with

characteristic speed equal to the particle velocity v). Thus, we choose the left state as the reference state if $v_L + v_R > 0$; otherwise, we choose the right state as the reference state. Additionally, if in the former case the slowest characteristic speeds are negative in both the left and right cells, we move the reference state to the constant state following this wave family. A similar move is made if the right state is the reference state and both of the fast speeds are positive. Next, we evaluate the flux at the reference state. Note that if for each wave family the characteristic speeds on the left and right have the same sign, then we are done.

If there is at least one transonic wave family, we compute the Engquist–Osher contribution to the flux computation. For simplicity, we assume that the initial reference state is the left state. Then we add to the flux at the left state an integral of the characteristic speed over those parts of the path where the characteristic speed is negative (if the reference state was moved to the first constant state, then the contribution of the first leg of the path to the integral is ignored):

$$f_{j+1/2}^{k+1/2} \doteq f(w_{j+1/2,L}^{k+1/2}) + \sum_{i=1}^{5} Xe_i \int_0^{a_i} \min\{\lambda_i, 0\}\, da_i.$$

A similar statement holds if the right state was the reference state, by considering parts of the path where the charac-

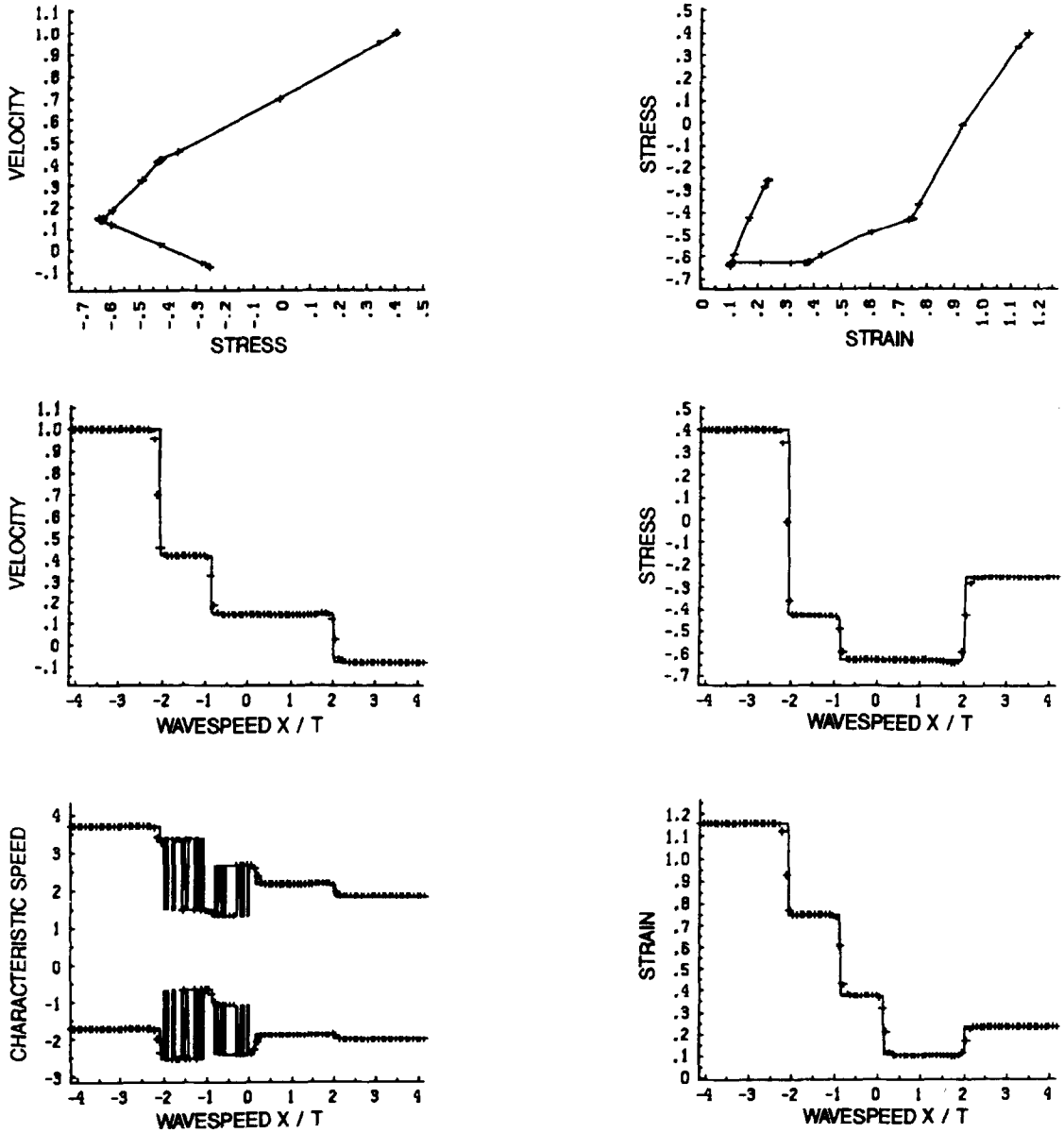

FIG. 3. Eulerian calculation with elastic and plastic rarefactions.

teristic speed is positive. The computation of the integral involves estimating the point at which the characteristic speed becomes zero. Using the pair of characteristic speeds for the same family from the cells on the left and right and assuming that this pair of characteristic speeds has opposite signs, we use linear interpolation between the two to estimate the expansion coefficient at which the characteristic speed should be zero. (Note that the use of a linear approximation to the characteristic speed is based on an assumption of no local extrema of the wavespeeds; if these are permitted by other choices of the model, then more elaborate representations of the characteristic speed must be used [1, 5].) We store the points along the leg of the path where the wavespeeds are negative or zero and evaluate the flux at these points, obtaining an approximation

$$Xe_i \int_0^{a_i} \min\{\lambda_i, 0\}\, da_i \doteq f(w_i^{\text{end}}) - f(w_i^{\text{begin}}).$$

Note that, since $\lambda_2 = \lambda_3 = \lambda_4 = \mathbf{v}$, we can combine the Engquist–Osher flux approximations for the linearly degenerate families. Thus the final numerical flux has the form

$$f_{j+1/2}^{k+1/2} = f(w_{j+1/2,\mathrm{L}}^{k+1/2}) + [f(w_1^{\text{end}}) - f(w_1^{\text{begin}})] + [f(w_{2-4}^{\text{end}}) - f(w_{2-4}^{\text{begin}})] + [f(w_5^{\text{end}}) - f(w_5^{\text{begin}})].$$

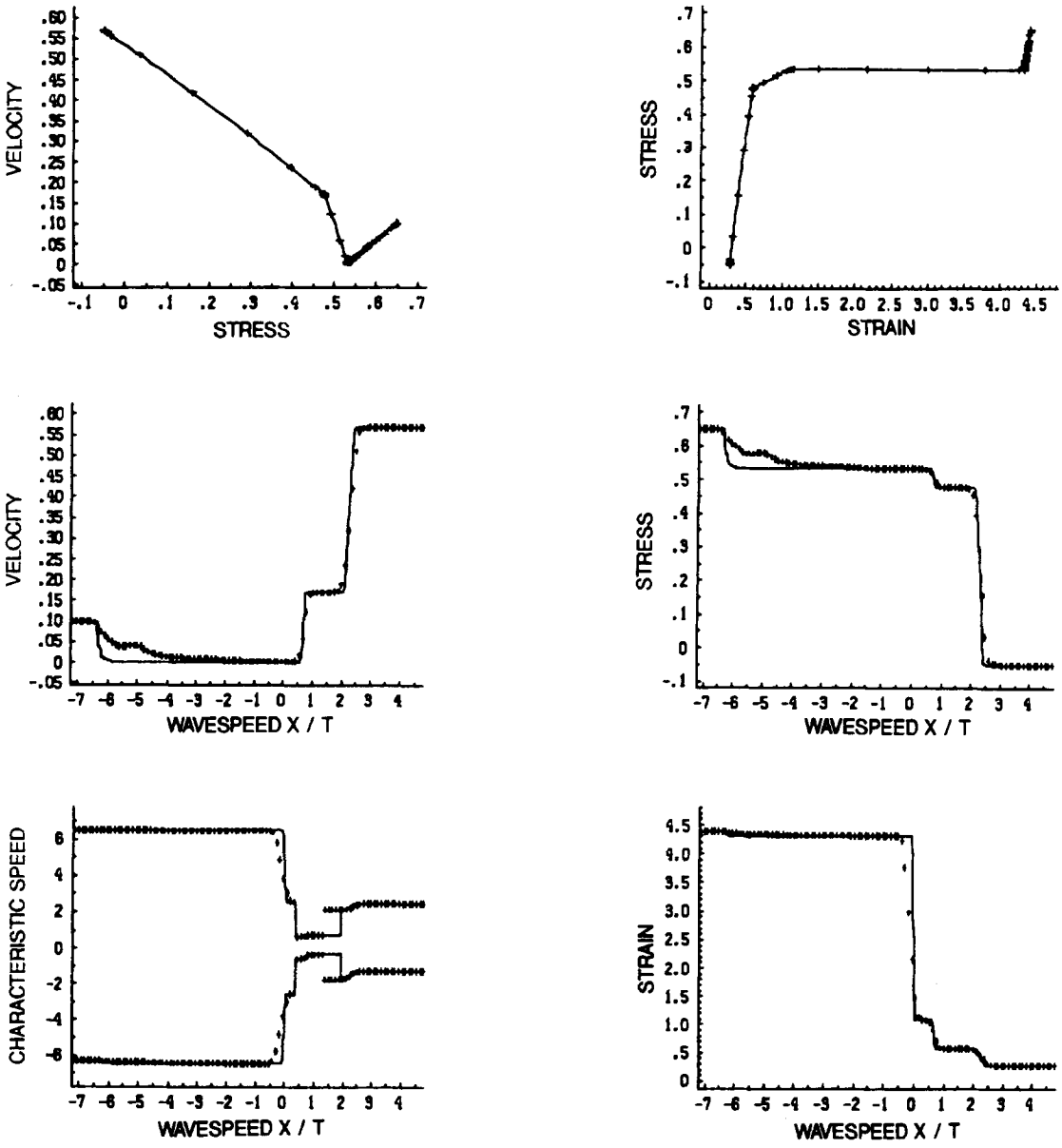

FIG. 4. Eulerian calculation with contact discontinuity stationary.

The final steps involve the conservative difference and stress update. These steps are similar to the Lagrangian case.

As numerical examples, we present the results of the same two problems studied in the Lagrangian case. In the first of the two examples (Fig. 3), the Eulerian algorithm resolves the shocks and contact discontinuities in two to three cells. On the other hand, the results on the second problem (Fig. 4) indicate that the Eulerian algorithm is not always so accurate. Here, the elastic shock moving left is highly smeared during startup and is not sufficiently strong to steepen itself into the typical two to three cell traveling discontinuity. We have performed this calculation twice: the first case in a frame of reference where the contact discontinuity is stationary, and the second in a frame of reference where all of the characteristic speeds are positive (see Fig. 5). Note that in the latter case, the exact solution of the Riemann problem is always given by the left state, so the poor performance of the algorithm is not due to the approximate Riemann solver. Rather, the inaccuracy is due to the interaction of the errors in capturing the contact discontinuity with the other waves during the early stages of the calculation. Because there is so little variation in the characteristic speed across the left-moving elastic shock, errors made in smearing the contact discontinuity can dominate the slight self-sharpening aspects of this weak

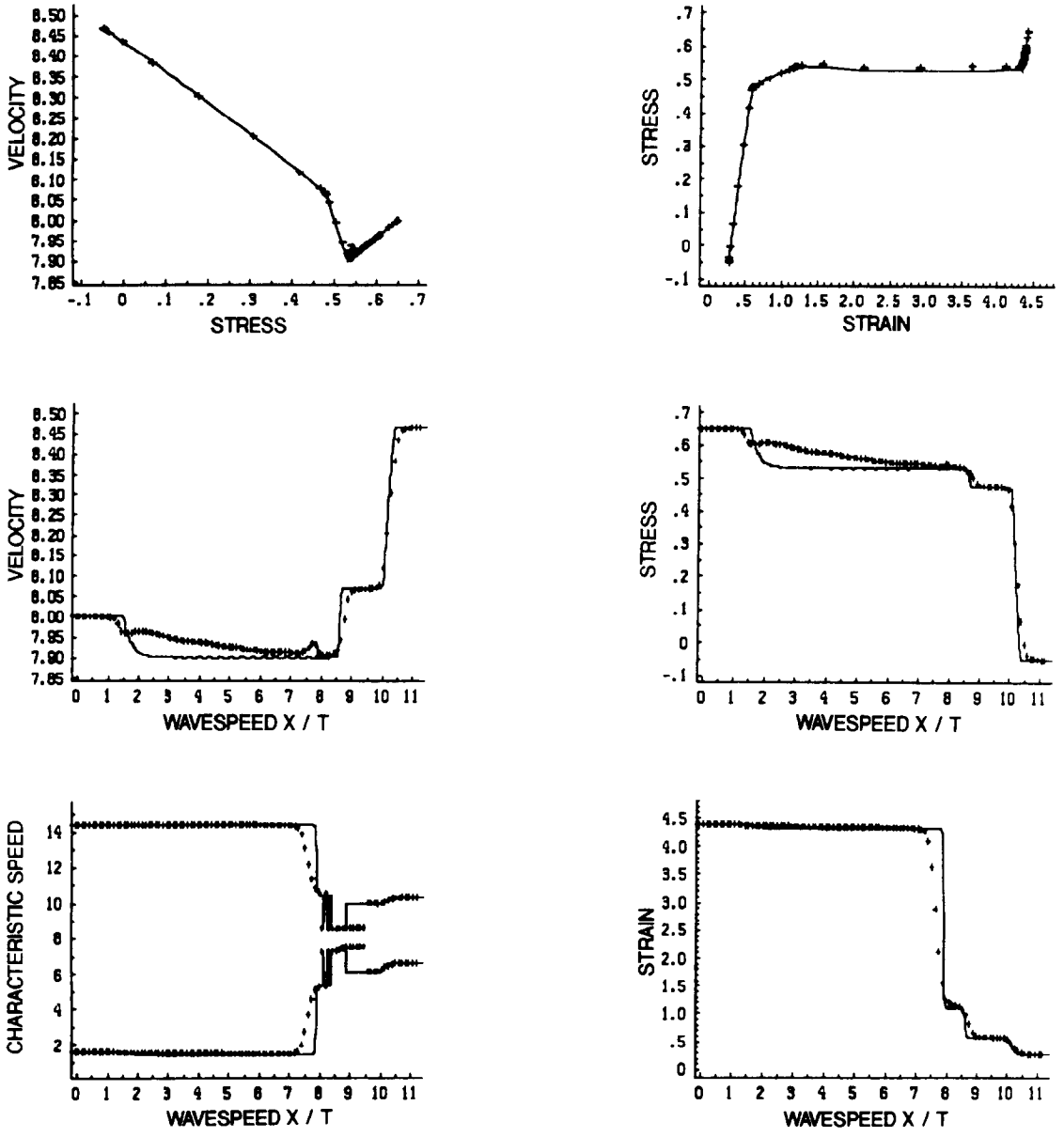

FIG. 5. Eulerian calculation with all characteristic speeds positive.

shock. When the contact discontinuity is tracked (as in a Lagrangian calculation), the waves are captured very nicely. This problem with contact discontinuities reducing the ability to capture other nonlinear waves in Eulerian calculations has also been noted in the context of enhanced oil recovery [1] and was shown in that case as well to be overcome with tracking of the contact discontinuity alone [18].

5. STRONG DISCONTINUITIES

Although we have not presented all of the results here, the Lagrangian and Eulerian higher-order Godunov algorithms using the weak-wave Riemann solvers discussed above have been tested on all 21 of the different kinds of solutions to the Riemann problem for the Antman–Szymczak model that were presented in [30]. The Eulerian algorithm worked well on all but two of the problems, where in each case it greatly smeared a weak shock because of the presence of a large contact discontinuity (see Figs. 4 and 5). On the other hand, the Lagrangian algorithm worked well on all of the problems except one involving a large change in characteristic speed, stress, and velocity across a shock. In this case, the second-order algorithm showed large oscillations behind the shock, which could be reduced but not removed by using the first-order algorithm. (See Fig. 6, which was run using the first-order algorithm at

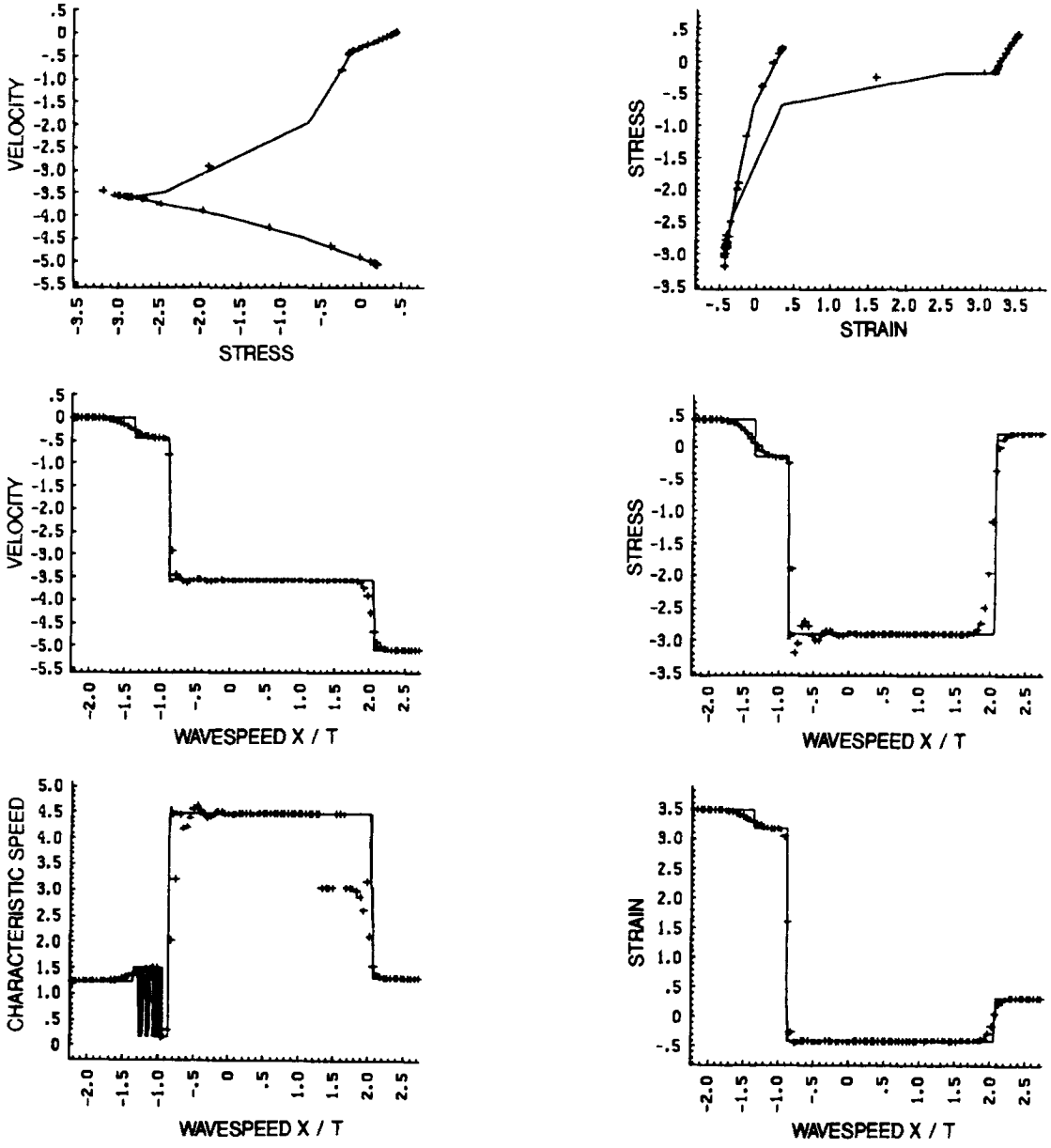

FIG. 6. First-order Godunov using weak-wave Riemann solver on strong shock.

CFL $= \frac{1}{2}$.) In this problem the left state is given by $\pi = 3.25$, $\varepsilon_L = 3.5$, and $\mathbf{v} = 0$, while the right is given by $\pi = 0.217$, $\sigma = 0.207$, and $\mathbf{v} = -5.081$. There are three waves in this example: an elastic shock precursing a strong plastic shock moving to the left, and a shock moving to the right. The difficulty in the Lagrangian algorithm derives from the coupling of the very large change in the plastic wavespeed across the plastic shock, with the large jumps in stress and velocity. This causes the weak-wave approximation of Section 3 to construct averages of the stresses and velocities in ways that do not correctly upwind the scheme. Let us discuss this point in greater detail.

Consider Rusanov's method [24]:

$$f_{j+1/2}^{k+1/2} = \{f(u_j^k) + f(u_{j+1}^k) - \lambda(u_{j+1}^k - u_j^k)\}\frac{1}{2}$$

$$= -\begin{bmatrix} \frac{1}{2}(\sigma_{j+1}^k + \sigma_j^k) + \frac{1}{2}\lambda(\rho_L \mathbf{v}_{j+1}^k - \rho_L \mathbf{v}_j^k) \\ \frac{1}{2}(\mathbf{v}_{j+1}^k + \mathbf{v}_j^k) + \frac{1}{2}\lambda((\varepsilon_L)_{j+1}^k - (\varepsilon_L)_j^k) \end{bmatrix}.$$

Here λ is an upper bound for the characteristic speeds along the path from u_j^k to u_{j+1}^k in the solution to the Riemann problem. When combined with a conservative difference, this method is a first-order upwind method and highly diffusive. For the strong shock example with the Antman–

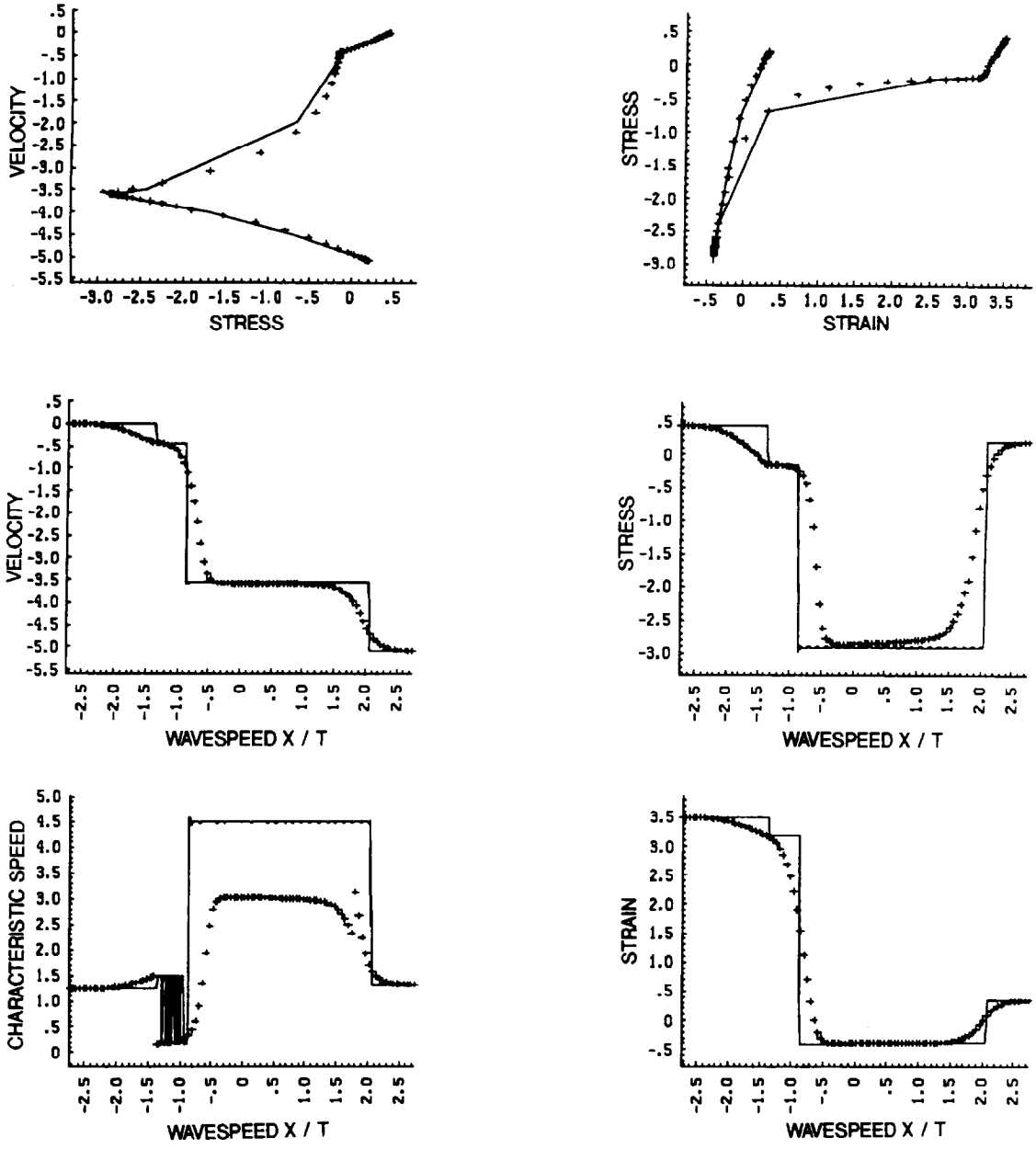

FIG. 7. Rusanov's method on strong shock.

Szymczak model, the Rusanov scheme produces highly smeared elastic and elastic–plastic shocks, but a somewhat better resolved plastic shock without numerical oscillations (see Fig. 7).

Next, we consider the weak-wave approximation used in our version of Godunov's method above. After computing the expansion coefficients, we find that our approximation to the flux at the solution of the Riemann problem is

$$f_{j+1/2}^{k+1/2} = f\left(w_j^{k+1/2} + \begin{bmatrix} 1 \\ \lambda_L \rho_L \end{bmatrix}_j^k a^-\right)$$
$$= -\begin{bmatrix} \left(\begin{matrix}(\sigma\lambda_L\rho_L)_{j+1}^k + (\sigma\lambda_L\rho_L)_j^k \\ + (\lambda_L\rho_L)_j^k\,(\lambda_L\rho_L)_{j+1}^k\,(\mathbf{v}_{j+1}^k - \mathbf{v}_j^k)\end{matrix}\right) \\ (\mathbf{v}\lambda_L\rho_L)_j^k + (\mathbf{v}\lambda_L\rho_L)_{j+1}^k + (\sigma_{j+1}^k - \sigma_j^k) \end{bmatrix}$$
$$\times \frac{1}{(\lambda_L\rho_L)_j^k + (\lambda_L\rho_L)_{j+1}^k}.$$

In the case where the left and right acoustic impedances are equal, i.e., $(\lambda_L\rho_L)_j^k = (\lambda_L\rho_L)_{j+1}^k = \lambda_L\rho_L$, this formula becomes

$$f_{j+1/2}^{k+1/2} = \begin{bmatrix} -\frac{1}{2}(\sigma_j^k + \sigma_{j+1}^k) - \frac{\lambda_L\rho_L}{2}(\mathbf{v}_{j+1}^k - \mathbf{v}_j^k) \\ -\frac{1}{2}(\mathbf{v}_j^k + \mathbf{v}_{j+1}^k) - \frac{\sigma_{j+1}^k - \sigma_j^k}{2\lambda_L\rho_L} \end{bmatrix}. \tag{5.1}$$

This has a form similar to Rusanov's and clearly adds a diffusion to the average flux. On the other hand, if $(\lambda_L\rho_L)_{j+1}^k \gg (\lambda_L\rho_L)_j^k$ (as at the strong shock in Fig. 6), the weak-wave approximation yields

$$f_{j+1/2}^{k+1/2} \approx \begin{bmatrix} -\sigma_j^k - (\lambda_L\rho_L)_j^k\,(\mathbf{v}_{j+1}^k - \mathbf{v}_j^k) \\ -\mathbf{v}_{j+1}^k - \dfrac{\sigma_{j+1}^k - \sigma_j^k}{(\lambda_L\rho_L)_{j+1}^k} \end{bmatrix}.$$

This upwinds the velocity and downwinds the stress, leading to numerical oscillations.

We will present two solutions to this problem, both of which can be generalized to problems involving shear. The first of the two methods uses a "strength-weighted average" of the characteristic speeds. This method produces reasonably good results for the test problems with the Antman–Szymczak model and is the only method that we have found to work successfully on the more realistic problem in Section 6. The second method makes some further modifications to the Riemann problem solution in order to guarantee that, at least at a strong discontinuity, the numerical flux is the Godunov flux plus a numerical dissipation.

The principal observation in both our approximate Riemann solvers for strong shocks is that the use of equal characteristic speeds for both the forward- and backward-moving characteristic directions makes the method more like Rusanov's. The natural approach is to construct some sort of average of the characteristic speeds found on either side of the cell edge where the flux is to be evaluated; in this way, the method is still accurate for weak waves. However, if the jump at the cell edge corresponds to a single wave, then we would prefer to use the characteristic speed and direction associated with this wave. Our first solution is to adopt a two-step approach to approximating the solution to the Riemann problem. First, we average the acoustic impedances $\lambda\rho$ on the left and the right,

$$(\overline{\lambda\rho})k_{j+1/2} = \tfrac{1}{2}(\lambda_j^k \rho_j + \lambda_{j+1}^k \rho_{j+1}),$$

and use this average to determine the expansion coefficients of the jump:

$$\begin{bmatrix} \bar{a}^- \\ \bar{a}^+ \end{bmatrix} = \begin{bmatrix} 1 & -1 \\ (\overline{\lambda\rho})_{j+1/2} & (\overline{\lambda\rho})_{j+1/2} \end{bmatrix}^{-1} \begin{bmatrix} \mathbf{v}_{j+1/2,\mathrm{R}}^{k+1/2} - \mathbf{v}_{j+1/2,\mathrm{L}}^{k+1/2} \\ \sigma_{j+1/2,\mathrm{R}}^{k+1/2} - \sigma_{j+1/2,\mathrm{L}}^{k+1/2} \end{bmatrix}.$$

Next, we construct a "strength-weighted average" of the acoustic impedances,

$$(\lambda\rho)_{j+1/2} = \frac{(\lambda\rho)_j^k\,|\bar{a}^-| + (\lambda\rho)_{j+1}^k\,|\bar{a}^+|}{|\bar{a}^-| + |\bar{a}^+|}.$$

We then use this average to construct revised values of the expansion coefficients and the solution to the Riemann problem. This approximate Riemann solver is generalized to problems involving shear by working with averages of the square roots of the acoustic tensors.

The numerical results with first-order Godunov using the strength-weighted averages are shown in Fig. 8. This strength-weighted average of the acoustic impedances allows the first-order Godunov method with the approximate Riemann solver to perform as well (at least for the Antman–Szymczak model) as first-order Godunov with the *analytic* Riemann solver (see Fig. 9). There are some small numerical oscillations just to the right of the strong plastic shock, even with the analytic Riemann solver. These appear to be due to the fact that the strong plastic shock is moving slowly (i.e., at a low CFL, since the timestep is dominated by the faster elastic speed at the stationary state), and so the dissipation of first-order Godunov is not sufficient to overcome the self-sharpening aspects of the strong shock. If, on the other hand, we solve the problem in an Eulerian frame of reference with all waves moving to the right, no significant numerical oscillations are detected (see Fig. 10).

Unfortunately, we are not able to show that the strength-

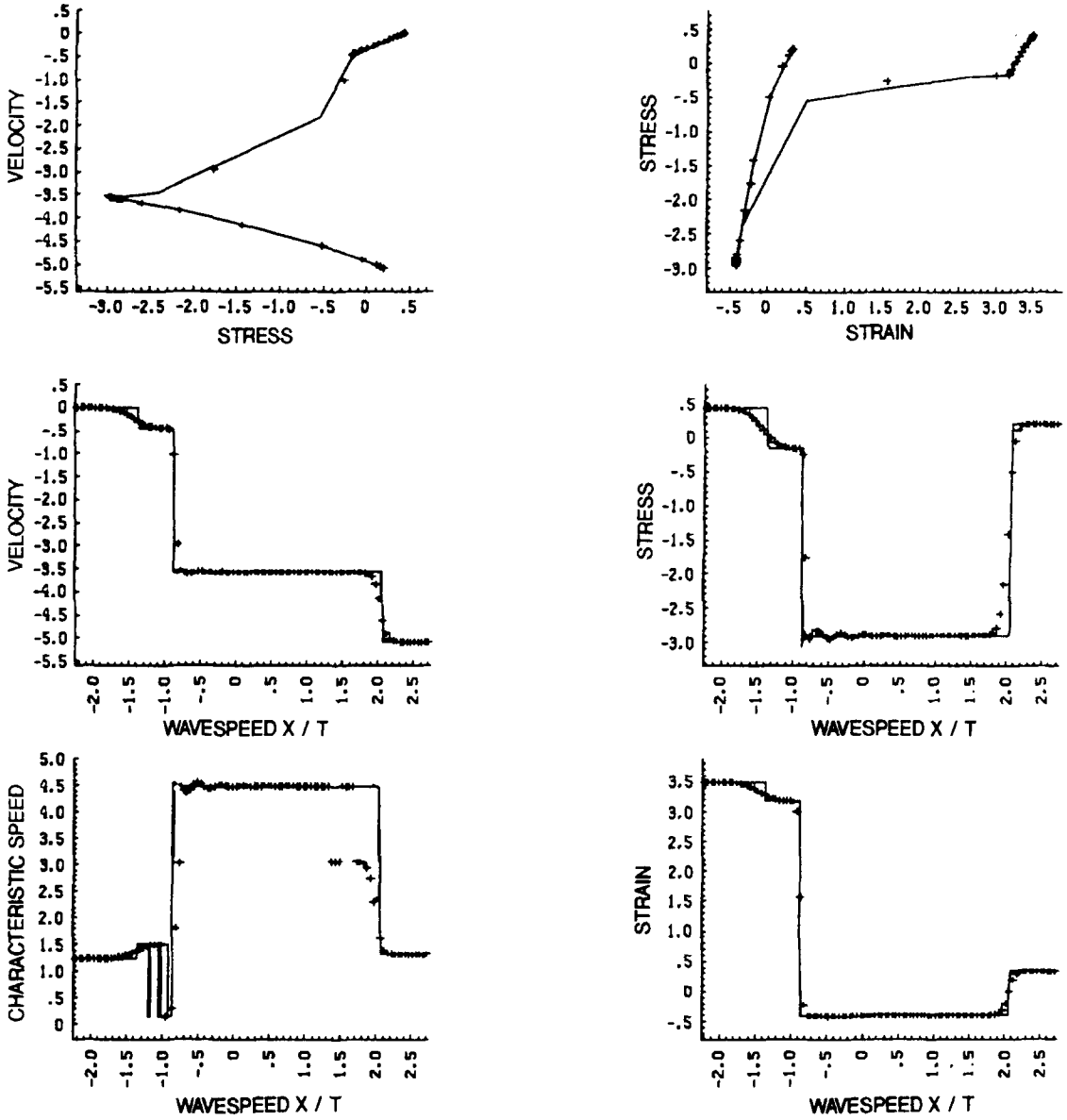

FIG. 8. First-order Godunov using strength-weighted average Riemann solver on strong shock.

weighted average, by itself, introduces sufficient numerical diffusion into the numerical method. Furthermore, the reasoning used to develop the strength-weighted average would suggest that averaging the acoustic tensors (i.e., $\lambda^2\rho^2$ instead of $\lambda\rho$) should work; in numerical experiments, this modification clearly does not work well. This suggests that we need to examine the numerical diffusion of the strength-weighted average in more detail.

To simplify the discussion of this issue, we will assume that we have a shock at edge $j+1/2$ moving to the left with speed $s<0$. Then the jump conditions for the shock are

$$-\begin{bmatrix}\sigma_{j+1}^k-\sigma_j^k\\ \mathbf{v}_{j+1}^k-\mathbf{v}_j^k\end{bmatrix}=\begin{bmatrix}(\rho_L)_{j+1/2}\,(\mathbf{v}_{j+1}^k-\mathbf{v}_j^k)\\ (\varepsilon_L)_{j+1}^k-(\varepsilon_L)_j^k\end{bmatrix}s.$$

Also, the flux given by the strength-weighted average is

$$\begin{bmatrix}\sigma\\ \mathbf{v}\end{bmatrix}_{j+1/2}^{k+1/2}=\begin{bmatrix}\sigma\\ \mathbf{v}\end{bmatrix}_{j+1}^{k}-\begin{bmatrix}1 & -(\lambda_L\rho_L)_{j+1/2}\\ -\dfrac{1}{(\lambda_L\rho_L)_{j+1/2}} & 1\end{bmatrix}\times\begin{bmatrix}\sigma_{j+1}^k-\sigma_j^k\\ \mathbf{v}_{j+1}^k-\mathbf{v}_j^k\end{bmatrix}\frac{1}{2}.$$

Thus, for a strong shock moving right, the strength-weighted average takes the form

$$\begin{bmatrix}\sigma\\ \mathbf{v}\end{bmatrix}_{j+1/2}^{k+1/2} = \begin{bmatrix}\sigma\\ \mathbf{v}\end{bmatrix}_{j+1}^{k} + \begin{bmatrix}(\lambda_L\rho_L)_{j+1/2} + s(\rho_L)_{j+1/2}\\ -\dfrac{s(p_L)_{j+1/2}}{(\lambda_L\rho_L)_{j+1/2}} - 1\end{bmatrix} \frac{1}{2}(\mathbf{v}_{j+1}^k - \mathbf{v}_j^k).$$

Here the Godunov flux is essentially the flux at the right; the strength-weighted average adds to this flux a term depending on the jump in velocity. Since the jump in velocity is negative (typically) for a shock, the correction to the Godunov flux avoids being antidiffusive, provided that the terms multiplying the velocity jump are nonnegative. In other words, diffusion is added to the Godunov stress if

$$(\lambda_L\rho_L)_{j+1/2} + s(\rho_L)_{j+1/2} > 0,$$

while diffusion is added to the Godunov velocity if

$$-\frac{s(\rho_L)_{j+1/2}}{(\lambda_L\rho_L)_{j+1/2}} - 1 > 0.$$

Thus, the strength-weighted average cannot add diffusion to both the stress and velocity simultaneously. Near a strong shock, the strength-weighted average will tend toward the

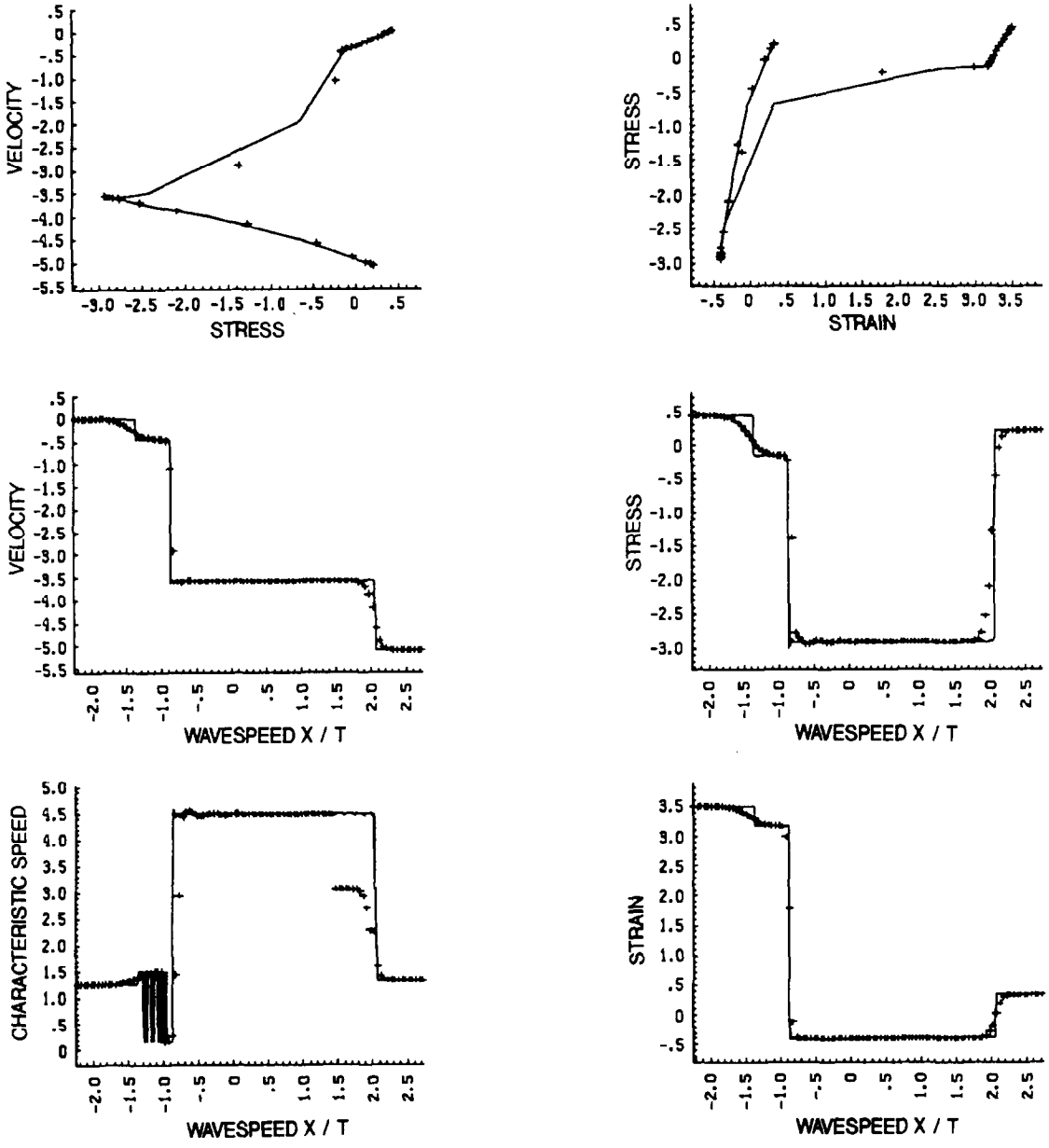

FIG. 9. First-order Godunov using exact Riemann solver on strong shock.

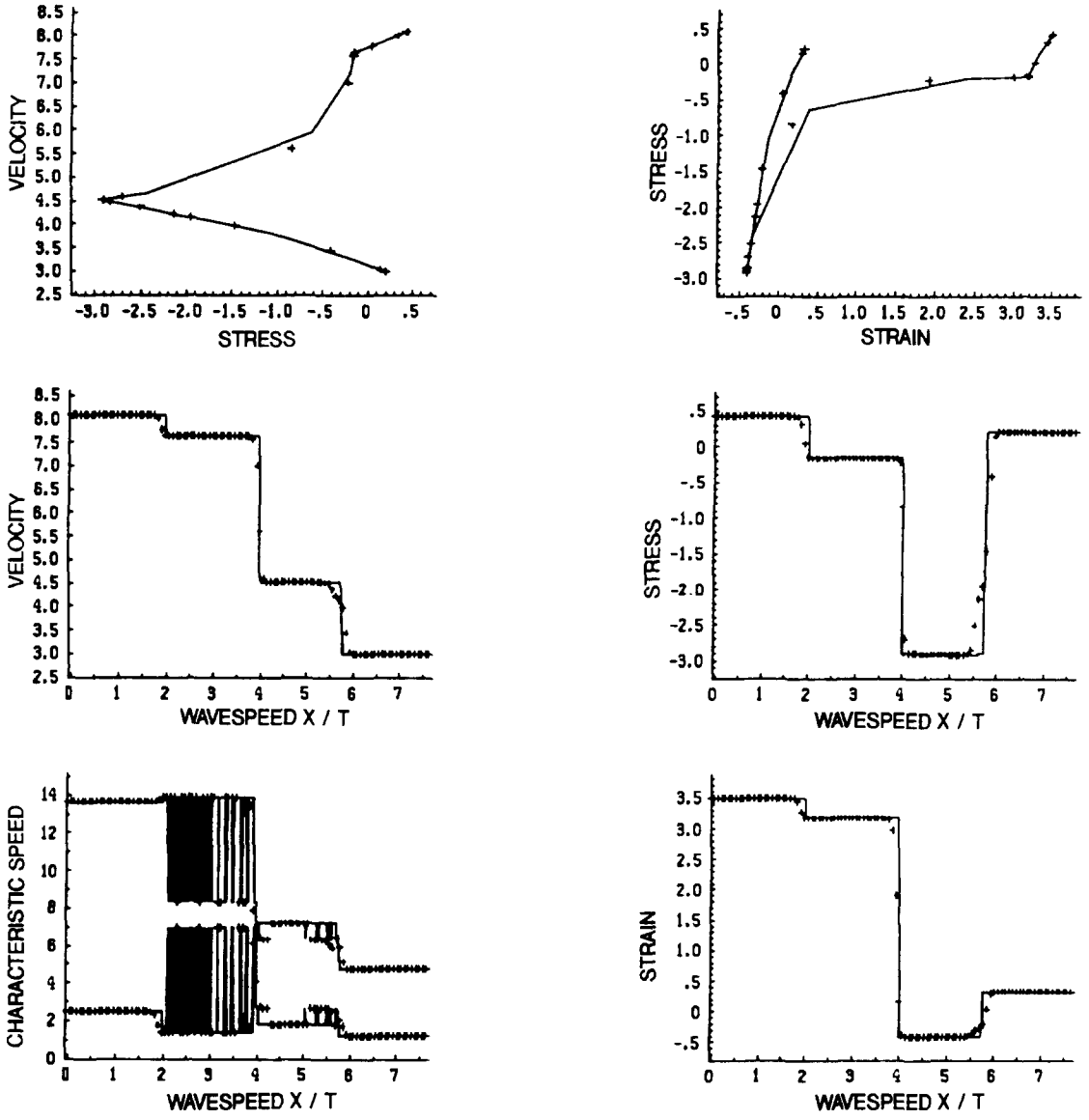

FIG. 10. Second-order Eulerian algorithm on strong shock.

pre-shock acoustic impedance, which is the smaller of the two; this will tend to add diffusion to the velocity component of the flux (i.e., equality of mixed partials) and antidiffusion to the stress component (i.e., the momentum equation). For typical impact problems, this is not necessarily a bad combination. Since the material bulk modulus (i.e., $\partial\sigma/\partial\varepsilon$) is typically large in the post-shock state, small oscillations in the displacement gradient will be greatly amplified in the stress; thus, a small amount of diffusion added to the Godunov velocity will contribute large damping to the stresses. On the other hand, the antidiffusion in the momentum equation, if small, can be overcome by other diffusive aspects of the Godunov method (e.g., averaging of the evolution operator).

In order to make sure that we have sufficient diffusion, we have constructed an alternative Riemann solver. We use different acoustic impedances in constructing the expansion coefficients of the jump, depending on whether we are determining the stress or the velocity component of flux. Thus, our approximate Riemann solver looks like

$$\begin{bmatrix}\sigma\\ \mathbf{v}\end{bmatrix}_{j+1/2}^{k+1/2} = \begin{bmatrix}\sigma\\ \mathbf{v}\end{bmatrix}_j^k + \begin{bmatrix} 1 & (\lambda_L\rho_L)^{\sigma}_{j+1/2} \\ \dfrac{1}{(\lambda_L\rho_L)^{\mathbf{v}}_{j+1/2}} & 1 \end{bmatrix} \begin{bmatrix}\sigma_{j+1}^k - \sigma_j^k\\ \mathbf{v}_{j+1}^k - \mathbf{v}_j^k\end{bmatrix}_j^k, \tag{5.2}$$

where the acoustic impedances satisfy

$$(\lambda_L \rho_L)^{\sigma}_{j+1/2} > |s|\,(\rho_L)_{j+1/2},$$
$$(\lambda_L \rho_L)^{\mathbf{v}}_{j+1/2} < |s|\,(\rho_L)_{j+1/2}.$$

In theory, the minimum and maximum of the acoustic impedances on either side of the discontinuity could be used to satisfy these inequalities; in practice, additional care must be taken. We construct an approximation to a local shock speed,

$$|s|^{k+1/2}_{j+1/2} = \left| \frac{\sigma^k_{j+1} - \sigma^k_j}{(\rho_L \mathbf{v})^k_{j+1} - (\rho_L \mathbf{v})^k_j} \right|,$$

which is unaffected by contact discontinuities (unlike the estimate in [16].) Then we take

$$(\rho_L)_{j+1/2} = \tfrac{1}{2}((\rho_L)_j + (\rho_L)_{j+1}),$$
$$(\lambda_L \rho_L)^{\sigma}_{j+1/2} = \min\{(\lambda_L \rho_L)^k_j, (\lambda_L \rho_L)^k_{j+1}, |s|^{k+1/2}_{j+1/2}(\rho_L)_{j+1/2}\},$$
$$(\lambda_L \rho_L)^{\mathbf{v}}_{j+1/2} = \max\{(\lambda_L \rho_L)^k_j, (\lambda_L \rho_L)^k_{j+1}, |s|^{k+1/2}_{j+1/2}(\rho_L)_{j+1/2}\}.$$

These acoustic impedances are then used in (5.2). In problems involving shear, we would construct the shock speed in the fastest wave family by looking at the jump in normal stress divided by the jump in normal velocity. We

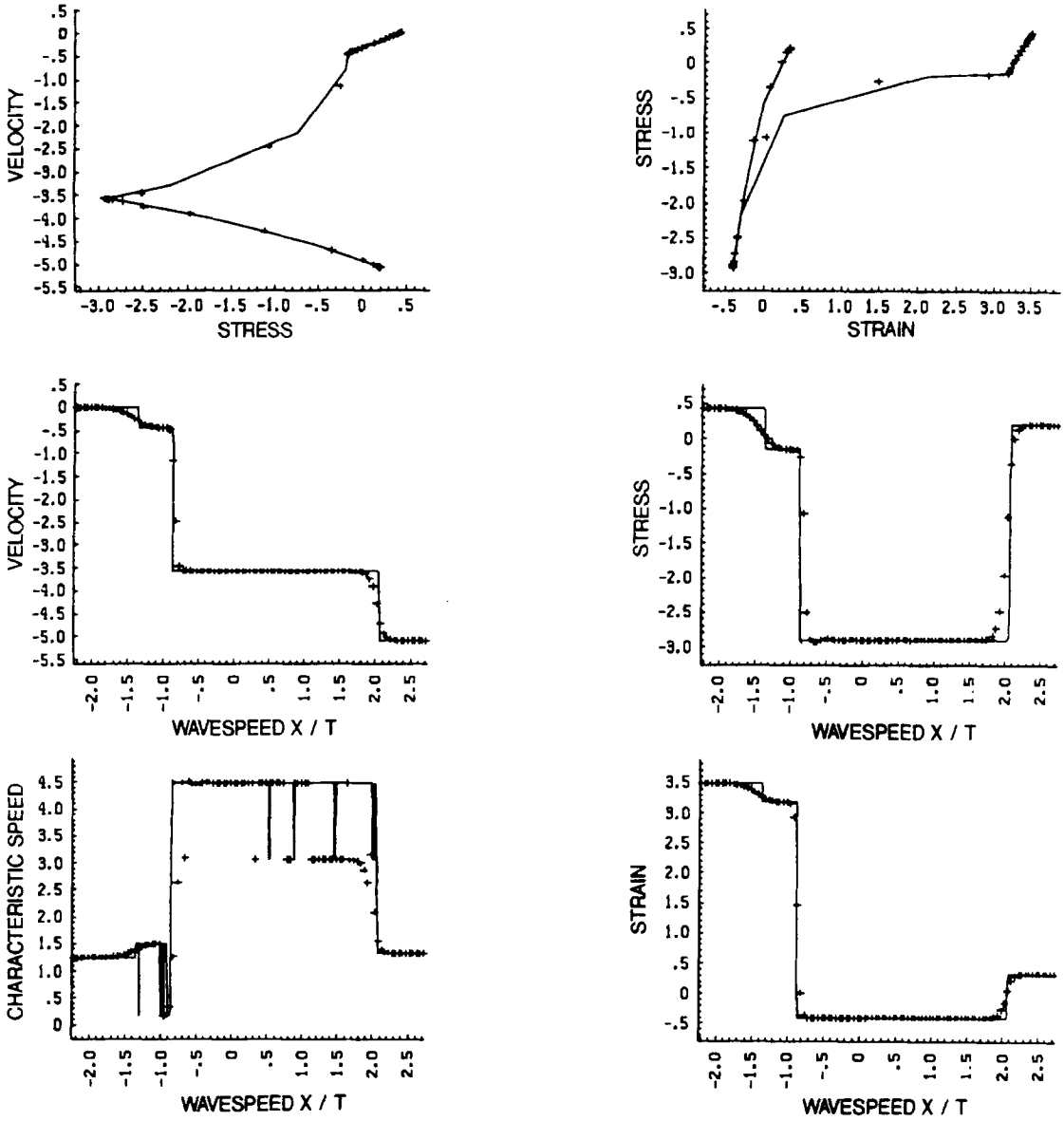

FIG. 11. First-order Lagrangian algorithm using strong diffusive Riemann solver.

would then construct the maximum and the minimum acoustic impedances for the fast wave and use them to overwrite the largest acoustic impedances of the original data.

Like Rusanov's method, this appoximate Riemann solver is highly diffusive; unlike Rusanov's method, it does not introduce diffusion at contact discontinuities. In order to prevent this Riemann solver from smearing weak shocks, we employ a strong discontinuity detector. For this purpose, we compute an estimate of the strength of the discontinuity and a strong discontinuity detector:

$$\zeta^k_{j+1/2} = \max\left\{\frac{|\sigma^k_{j+2} - \sigma^k_{j-1}|}{((\lambda_L)^k_j)^2 (\rho_L)_j}, \frac{|\mathbf{v}^k_{j+2} - \mathbf{v}^k_{j-1}|}{(\lambda_L)^k_j}\right\},$$

$$\eta^k_{j+1/2} = \min\left\{\max\left\{\frac{\zeta^k_{j+1/2} - \zeta_{\min}}{\zeta_{\max} - \zeta_{\min}}, 0\right\}, 1\right\}.$$

If $\eta^k_{j+1/2}$ is equal to 1, the discontinuity is considered to be strong and the approximate Riemann solver for strong discontinuities is used; if it is equal to 0, the weak-wave approximation is used. For discontinuities of intermediate strength, we use $\eta^k_{j+1/2}$ to average between the weak and strong fluxes. In addition, if $\eta^k_{j+1/2} > 0$ we set the slopes to zero in the characteristic tracing step. For the computations in this paper, we took $\zeta_{\min} = \frac{1}{4}$ and $\zeta_{\max} = \frac{1}{2}$. We also used the elastic speeds in the denominators of $\zeta^k_{j+1/2}$.

In summary, the strength-weighted Riemann solver has the advantage of using no user-controlled parameters, but it occasionally produces some small overshoots during startup, and it is not necessarily at least as diffusive as Godunov's method with the exact Riemann solver. The other approximate Riemann solver for strong shocks can be

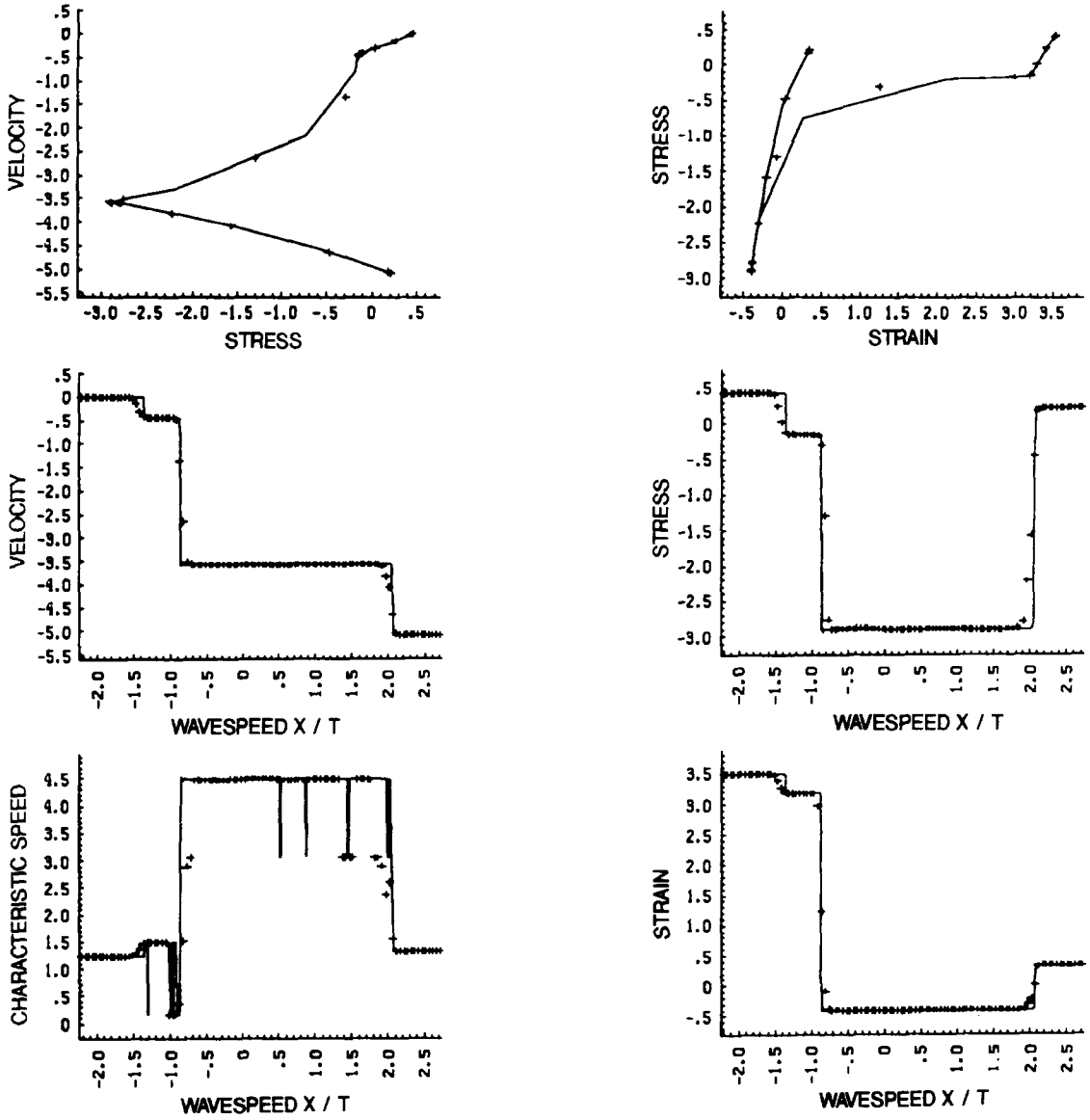

FIG. 12. Second-order Lagrangian algorithm on strong shock.

shown to be at least as diffusive as Godunov's method for a single discontinuity, but it does involve two user-controlled parameters to turn it off away from strong discontinuities. This second Riemann solver produces better overall results than the strength-weighted averages for the Antman–Szymczak model, but does not work well for the model in the next section (see Fig. 11).

These approximate Riemann solvers have greatly improved the first-order Godunov algorithm. However, no matter which Riemann solver we use, the second-order Godunov algorithm would still produce significant numerical oscillations near strong discontinuities. This is because the small amount of numerical diffusion introduced by the second-order Godunov method is more than overcompensated by the compression of the shock. The result is that shocks become "too sharp," with one or no points in the discontinuity and oscillations before or after the shock.

A solution is to reduce the method to first-order near sharp discontinuities. Accordingly, we have introduced a revised form of "slope flattening" suggested by Colella [8]. Sharp discontinuities can be detected by jumps in stress or velocity two cells apart that are essentially the same as jumps four cells apart. (In problems involving shear, we look at jumps in pressure and normal velocity.) We compute

$$\omega_j = \max\left\{0, \min\left\{1, \frac{0.85 - \dfrac{\sigma_{j+1}^k - \sigma_{j-1}^k}{\sigma_{j+2}^k - \sigma_{j-2}^k}}{0.1}, \frac{\mathbf{v}_{j+2}^k - \mathbf{v}_{j-2}^k}{0.1}\right\}\right\}. \tag{5.3}$$

(Here, the constants 0.85 and 0.1 have been determined experimantally and are not adjusted in practice.) Afterward, we multiply the limited slopes $\Delta c_j^{\pm}$ by $\min\{\omega_{j-1}, \omega_j, \omega_{j+1}\}$ in order to introduce additional numerical diffusion in cells near a sharp discontinuity.

In Fig. 12 we show the result of a second-order Godunov Lagrangian calculation using the second Riemann solver for strong shocks and slope flattening. Note that the shocks are now resolved in two to three cells.

6. APPLICATION TO REALISTIC MATERIAL MODELS

In the preceding sections, we have described second-order Godunov methods for the Antman–Szymczak model in Lagrangian and Eulerian frames of reference. This material model is useful for theoretical purposes, but does not describe the response of realistic materials. The purpose of studying second-order Godunov methods applied to this model has been to develop the numerical methods on problems with known answers. Our goal in this section is to apply the techniques developed for the Antman–Szymczak model to a plasticity model of practical interest, involving the effect of a high-explosive pressure load on the interior of a clay sphere. This next problem will involve a different material model.

The cap model [25] is a well-known model for the deformation of soils and rock. It consists of a system of ordinary differential equations for the components of the stress tensor and a history parameter, with the system being constrained by plastic yield conditions:

$$\frac{dy}{d\tau} = g(y, D), \qquad \phi(y) \leqslant 0.$$

Here,

$$y = \begin{bmatrix} S' \\ p \\ \varepsilon \end{bmatrix}$$

is a vector consisting of the deviatoric stress, the pressure, and a history parameter $\varepsilon(\chi)$ representing the plastic volumetric strain as a function of the location of the movable cap. Also,

$$\phi(S', p, \chi) = \|S'\| - F(p, \chi)$$

represents the yield conditions. Finally, D is the symmetric part of the velocity gradient (i.e., the strain rate). One of us has already described the implementarion of a second-order integration technique for this model [28]. He showed how

[redacted]

model differential algebraic equations in order to obtain a fully second-order algorithm and applied the combined algorithm to several problems involving weak to moderate waves. In this paper, we want to apply the model to a problem involving a strong shock in spherical symmetry.

For the spherical explosion problem, the cap model functions are the same as in [28], except that the model parameters are different, and the bulk modulus is strongly nonlinear. The nonlinearity in the bulk modulus is designed to represent the softness of the initial material containing 3% air voids, relative to its compressed state in which the air voids are gone and the material grains "lock up." The cap model parameters are

$$A = 0.115 \text{ Mpa}, \qquad B = -1.89 \text{ Mpa}^{-1},$$
$$C = 0.095 \text{ Mpa}, \qquad d = -0.6 \text{ Mpa}^{-1},$$
$$R = 2.5, \qquad w = 0.03, \qquad X_0 = 0,$$
$$\mu = 300 \text{ Mpa}, \qquad \rho = 1969 \text{ kg/m}^3$$

The bulk modulus takes the form

$$\kappa = 8000. + 70. \times \max\{p, 0\}^{0.7} \text{ Mpa},$$

where the pressure p also has units of Mpa. The boundary

condition at the inner radius takes the form of an incoming wave with known radial stress, given by the pressure of the explosive gases. This is specified by the JWL equation of state

$$p = 7.5807 \times 10^5 \times \exp(-4.9\zeta) + 0.08513 \times 10^5 \exp(-1.1\zeta) + 0.01143 \times 10^5 \times \zeta^{-1.2}.$$

Here, ζ is the ratio of the current volume of the explosive products (i.e., the inner cavity) to its initial radius. The inner radius is at 0.2947 m, and the outer radius is at 3.5m. The clay is initialized with an infinitesimal cap, corresponding to $\chi = -0.013972$ Mpa. Thus, the material is initially at yield.

Now that we have outlined the stress–strain relationship, let us return to the equations of motion. In order to describe these equations in spherical symmetry, we will introduce some notation. The (Eulerian) Cauchy stress tensor takes the form

$$S_E = \begin{bmatrix} S_{rr} & 0 & 0 \\ 0 & S_{\theta\theta} & 0 \\ 0 & 0 & S_{\theta\theta} \end{bmatrix},$$

so the (Lagrangian) first Piola–Kirchhoff stress tensor is

$$\begin{bmatrix} Z_{rr} & 0 & 0 \\ 0 & Z_{\theta\theta} & 0 \\ 0 & 0 & Z_{\theta\theta} \end{bmatrix} = \begin{bmatrix} S_{rr}(x_r/r)^2 & 0 & 0 \\ 0 & S_{\theta\theta}(x_r/r)(\partial x_r/\partial r) & 0 \\ 0 & 0 & S_{\theta\theta}(x_r/r)(\partial x_r/\partial r) \end{bmatrix},$$

where x_r is the current (Eulerian) particle position and r is the original (Lagrangian) particle position. Then conservation of momentum can be written in the Lagrangian form

$$\rho_L r^2 \frac{d\mathbf{v}_r}{\partial\tau} - r^2 \frac{\partial Z_{rr}}{\partial r} - 2(Z_{rr} - Z_{\theta\theta})r = 0,$$

or in a form that uses Cauchy stress in the Lagrangian frame,

$$\rho_L r^2 \frac{d\mathbf{v}_r}{\partial\tau} - x_r^2 \frac{\partial S_{rr}}{\partial r} - 2(S_{rr} - S_{\theta\theta}) \frac{\partial^{(1/2)} x_r^2}{\partial r} = 0.$$

The Lagrangian equation has the quasilinear form

$$\frac{\partial}{\partial\tau}\begin{bmatrix} \mathbf{v} \\ Z_{rr} \end{bmatrix} + \begin{bmatrix} \dfrac{1}{\lambda_L\rho_L} & -1 \\ \lambda_L\rho_L & \lambda_L\rho_L \end{bmatrix}\begin{bmatrix} -\lambda_L & 0 \\ 0 & \lambda_L \end{bmatrix} \times \begin{bmatrix} \dfrac{1}{\lambda_L\rho_L} & -1 \\ \lambda_L\rho_L & \lambda_L\rho_L \end{bmatrix}^{-1} \frac{\partial}{\partial r}\begin{bmatrix} \mathbf{v} \\ Z_{rr} \end{bmatrix} = \begin{bmatrix} 2((Z_{rr} - Z_{\theta\theta})/\rho_L)(1/r) \\ (h_{r\theta}/\rho_L)(\mathbf{v}/r) \end{bmatrix}$$

and is differenced in the form

$$[\mathbf{v}_j^{k+1} - \mathbf{v}_j^k]\,\rho_j \frac{1}{3}[r_{j+1/2}^3 - r_{j-1/2}^3] - \Delta\tau\,[(Z_{rr})_{j+1/2}^{k+1/2} - (Z_{rr})_{j-1/2}^{k+1/2}]\frac{1}{3}[r_{j+1/2}^3 - r_{j-1/2}^3] - 2\Delta\tau\left[\frac{(Z_{rr})_j^{k+1} + (Z_{rr})_j^k}{2} - \frac{(Z_{\theta\theta})_j^{k+1} + (Z_{\theta\theta})_j^k}{2}\right] \times \frac{1}{2}[r_{j+1/2}^2 - r_{j-1/2}^2] = 0. \tag{6.1}$$

On the other hand, the form employing the Cauchy stress has the quasilinear form

$$\frac{\partial}{\partial\tau}\begin{bmatrix} \mathbf{v} \\ S_{rr} \end{bmatrix} + \begin{bmatrix} \dfrac{1}{\lambda_E\rho_E} & -1 \\ \lambda_E\rho_E & \lambda_E\rho_E \end{bmatrix}\begin{bmatrix} -\lambda_L & 0 \\ 0 & \lambda_L \end{bmatrix} \times \begin{bmatrix} \dfrac{1}{\lambda_E\rho_E} & -1 \\ \lambda_E\rho_E & \lambda_E\rho_E \end{bmatrix}^{-1} \frac{\partial}{\partial r}\begin{bmatrix} \mathbf{v} \\ S_{rr} \end{bmatrix} = \begin{bmatrix} 2((S_{rr} - S_{\theta\theta})/\rho_L)(\partial(1/2)\,x^2/\partial(1/3)r^3) \\ (\tilde{h}_{r\theta}/\rho_L)(\mathbf{v}/\mathbf{x}) \end{bmatrix}$$

and is differenced in the form

$$[\mathbf{v}_j^{k+1} - \mathbf{v}_j^k]\,\rho_j \frac{1}{3}[r_{j+1/2}^3 - r_{j-1/2}^3] - \Delta\tau\,[(S_{rr})_{j+1/2}^{k+1/2} - (S_{rr})_{j-1/2}^{k+1/2}] \times \frac{1/3[(x_{j+1/2}^{k+1/2})^3 - (x_{j-1/2}^{k+1/2})^3]}{x_{j+1/2}^{k+1/2} - x_{j-1/2}^{k+1/2}} - 2\Delta\tau\left[\frac{(S_{rr})_j^{k+1} + (S_{rr})_j^k}{2} - \frac{(S_{\theta\theta})_j^{k+1} + (S_{\times\theta})_j^k}{2}\right] \times \frac{1}{2}[(x_{j+1/2}^{k+1/2})^2 - (x_{j-1/2}^{k+1/2})^2] = 0. \tag{6.2}$$

Here, $\tilde{h}_{r\theta}$ is derived from the cap model, and

$$h_{r\theta} = (\tilde{h}_{r\theta} + 2S_{rr})\frac{x}{r},$$

$$\lambda_E = \lambda_L \frac{\partial x}{\partial r},$$

$$\lambda_L\rho_L = \lambda_E\rho_E\left(\frac{x}{r}\right)^2.$$

The quantities at the half-time level are determined by characteristic tracing and the formula

$$x_{j+1/2}^{k+1/2} = x_{j+1/2}^k + \tfrac{1}{2}\Delta\tau v_{j+1/2}^{k+1/2} = \tfrac{1}{2}(x_{j+1/2}^k + x_{j+1/2}^{k+1});$$

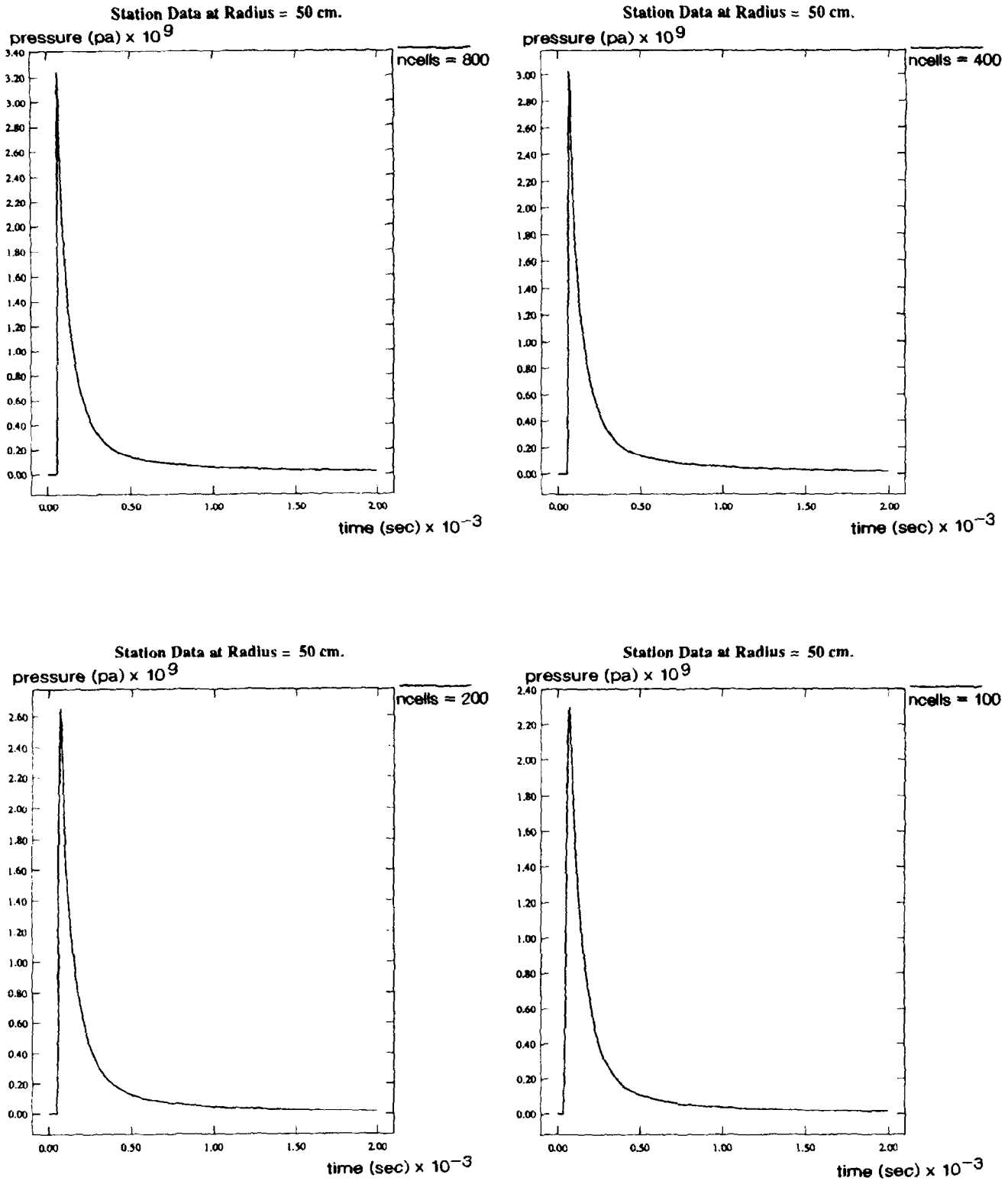

FIG. 13. Mesh refinement study for pressure time history at $r = 50$ cm.

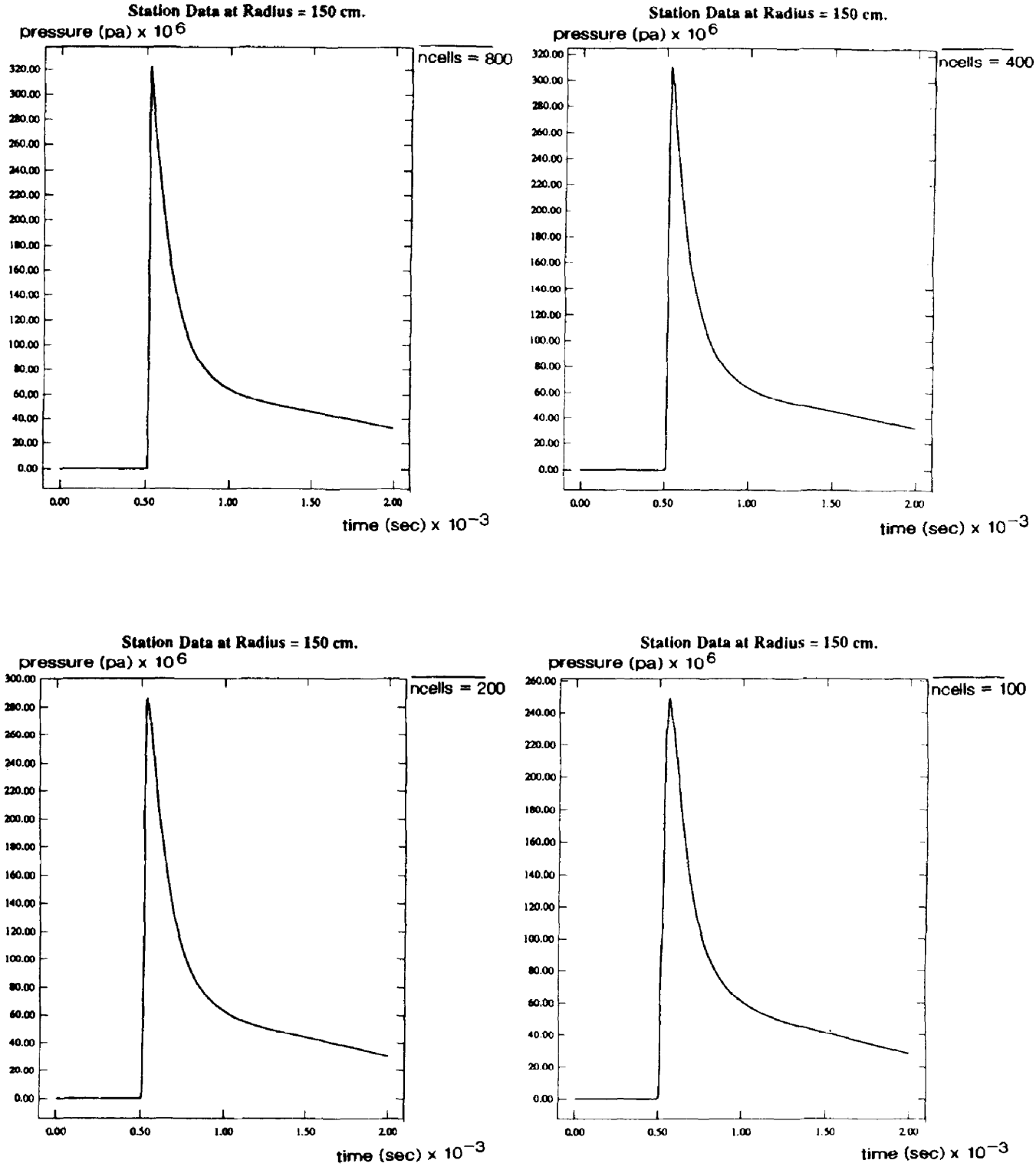

FIG. 14. Mesh refinement study for pressure time history at $r = 150$ cm.

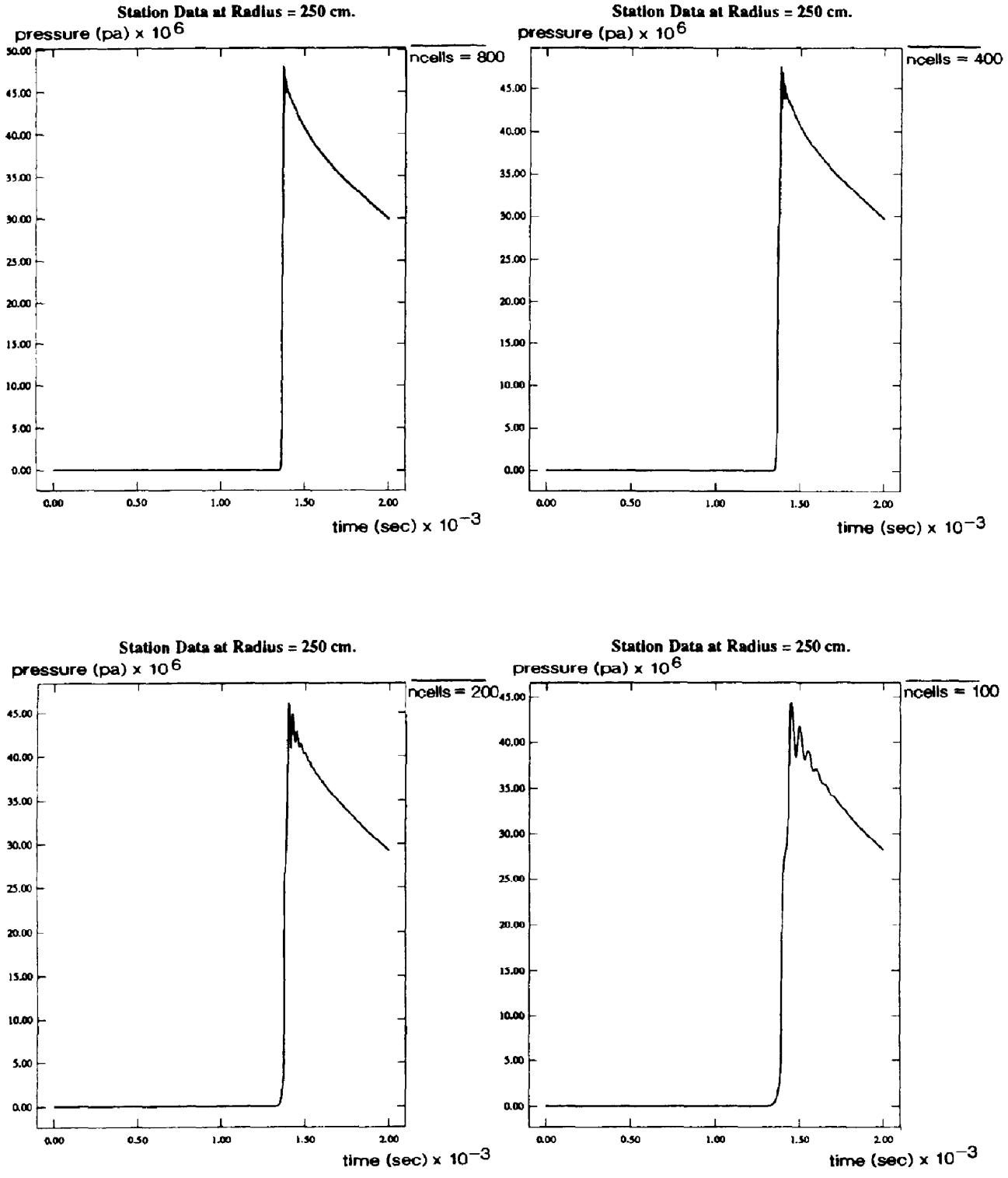

FIG. 15. Mesh refinement study for pressure time history at $r = 250$ cm.

furthermore, the stresses at the new time level are computed by the cap model algorithm before the velocity update.

We used the difference scheme (6.2) instead of (6.1) for two reasons. For one, (6.2) has a linearized coefficient matrix that uses the Eulerian acoustic impedances for the charactersitic directions, while the other uses the Lagrangian acoustic impedances. Near the explosion, the stiffening of the material and the compression of the Eulerian width of the Lagrangian cell lead to significant increases in the Lagrangian acoustic impedances, while the Eulerian acoustic impedances are nicely behaved. Second, [illegible] Kirchhoff stress at zero Lagrangian radius is not well defined.

In attempting to compute the solution to this explosion problem, we encountered a number of difficulties. First of all, the weak-wave Riemann solver produced serious numerical oscillations that eventually led to tensile failure of the material and premature termination of the simulation, so it had to be replaced with one of the Riemann solvers for strong shocks. Second, we found that the attenuation of the peak pressure as the shock moved out to larger radii caused the strong shock detector eventually to turn off, unless the parameters $\zeta_{\min}$ and $\zeta_{\max}$ were set so low that essentially all disturbances at early time appeared to be strong discontinuities; as a result, we could not use the second of the two approximate Riemann solvers for strong shocks. Our third problem was that the peak pressure and peak velocities occurred in different cells; as a result, slope limiting tended to limit the two fields differently, resulting in numerical oscillations with the second-order algorithm.

In order to make the second-order Godunov method work on this problem, it has been necessary to employ a number of numerical techniques. In order to handle the first two difficulties, we used strength-weighted averages for the approximate Riemann problem. The third problem was treated by computing slopes in the flux variables (radial stress and velocity), computing the factors by which standard limiting wants to reduce the centered slopes, and then limiting both centered slopes by the minimum of these two factors.

The results in Figs. 13–15 show the pressure histories at three particles, one near the inner radius, one in the middle, and the other near the outer radius. The four plots in each of these figures show mesh refinement studies, at CFL $= \frac{1}{2}$, using uniform grid calculations on 100, 200, 400, or 800 cells. Note that the pressure peaks are unresolved with 400 cells or fewer and that there are numerical oscillations at large radii for all of the calculations. (These oscillations occur even when the first-order version of the algorithm is used.) We remark that the second-order algorithm improves the height of the pressure peaks at the inner stations in the coarse uniform grid calculations by roughly 10%, relative to calculations with the first-order version of the algorithm. However, the second-order algorithm does not make a significant difference in the accuracy of the results for stations at the large radii.

A significant amount of work was performed to determine the cause of the oscillations at the outer station. We had suspected that the difficulty was due to the fact that at late time the timestep was being determined by the very large wavespeeds that developed in the highly crushed cells near the explosive; at late time, this meant that the shock was being captured at a very low local value of CFL. In such circumstances, the Godunov method introduces essentially [illegible] strong shocks may experience insufficient dissipation to prevent numerical oscillations. In order to test our hypothesis, we constructed an adaptive mesh refinement algorithm, which was specially designed to allow the refined mesh to use as large an integral fraction of the coarse grid timestep as the fine grid CFL constraint would allow. Calculations with the adaptive mesh refinement algorithm showed that the uniform grid calculations with 800 cells are essentially converged. Unfortunately, this adaptive mesh refinement algorithm did not remove the numerical oscillations at late time. Next, we tried subcycling the cap model integration, taking as many as 50 timesteps for the equation of state integration for each fine grid timestep. This reduced the oscillations somewhat, but did not completely eliminate them. Numerical tests indicate that there is significant error in the cap model integration at the shock for pressures near the point where the first-order Taylor expansion of the failure envelope was indistinguishable from a constant to the working accuracy of a CRAY XMP. Thus, our current hypothesis is that these numerical oscillations are due to a peculiar sensitivity of the clay cap model to numerical roundoff errors.

7. SUMMARY

In this paper we extended our previous work on modeling of non-linear waves in elastic–plastic solids in two ways. First, we constructed an Eulerian version of the algorithm, which required a significantly more complicated method for the approximate solution of Riemann problems. Second, we constructed two alternative techniques for modifying the weak-wave approximation to the solution of the Riemann problem, in order to handle strong discontinuities. Our numerical methods were verified by comparison with a complete set of analytical solutions to the Riemann problem for the Antman–Szymczak model, and the resulting algorithm was used to solve a very difficult applied problem modeling an explosion inside a clay sphere. These results represent the final necessary steps before extending the Godunov algorithm to multi-dimensional problems.

The application of the Lagrangian algorithm to the explosion problem represents a great deal of work, because

the numerical techniques developed for gas dynamics and for the Antman–Szymczak model did not work without modification. The early numerical results provided only limited information, because numerical oscillations typically made the cap model fail in tension, terminating the calculation. We had to proceed slowly, testing each piece of the algorithm because each was equally suspect. The discussion of the modifications needed to make the algorithm work provide some useful insight, however. The list of problems roughly follows the sequence in which they appear during the calculation. By plotting the numerical fluxes as a function of timestep, we were able to detect the difficulties with the approximate Riemann solvers at early time. Other difficulties were more localized and were detected by plotting profiles of the solution across the grid.

We believe that the results in this paper illustrate that, while many modern shock-capturing methods work well on shock-tube problems for gamma-law gases, this does not mean that they will apply to other problems just as easily. Some new applications, such as shocks in solids, may require a significant amount of refinement of the numerical algorithm by experts trained in both the applications and the algorithms.

ACKNOWLEDGMENTS

We thank Phil Colella (Mechanical Engineering Department, University of California at Berkeley) for several thoughtful conversations regarding Godunov methods during the course of this work. We would also like to acknowledge (thank is not the proper word) Joe Zelasko (Geomechanics Division, U. S. Army Corps of Engineers Waterways Experiment Station, Vicksburg, MI) for suggesting the problem, and Ivan Sandler) Weidlinger Associates, New York, NY) for useful conversations regarding the cap model.

REFERENCES

1. M. B. Allen III, A. Behie, and J. A. Trangenstein, *Multi-Phase Flow in Porous Media: Mechanics, Mathematics and Numerics*, Lecture Notes in Engineering, Vol. 34 (Springer-Verlag, New York/Berlin, 1988).
2. S. S. Antman and W. G. Szymczak, *Contemp. Math.* **100**, 27 (1989).
3. K.-J. Bathe and E. L. Wilson, *Numerical Methods in Finite Element Analysis* (Prentice-Hall, Englewood Cliffs, NJ, 1976).
4. Z. P. Bazant, *J. Appl. Mech.* **38**, 919 (1971).
5. J. B. Bell, P. Colella, and J. A. Trangenstein, *J. Comput. Phys.* **82**, 362 (1989).
6. T. Belytschko and T. J. R. Hughes (Eds.), *Computational Methods for Transient Analysis, Computational Methods in Mechanics*, Vol. 1, (North-Holland, Amsterdam, 1983).
7. J. P. Boris and D. L. Book, *J. Comput. Phys.* **20**, 397 (1976).
8. P. Colella, *SIAM J. Sci. Stat. Comput.* **6**, 104 (1985).
9. P. Colella, *J. Comput. Phys.* **87**, 171 (1990).
10. P. Colella and P. R. Woodward, *J. Comput. Phys.* **54**, 174 (1984).
11. N. Cristescu, *Dynamic Plasticity* (North-Holland, Amsterdam, 1967).
12. C. M. Dafermos, *J. Differential Eqs.* **14**, 202 (1973).
13. B. Engquist and S. Osher, *Math. Comput.* **34**, 45 (1980).
14. A. Harten, *SIAM J. Numer. Anal.* **21**, 174 (1984).
15. A. Harten, *J. Comput. Phys.* **83**, 148 (1989).
16. A. Harten, P. D. Lax, and B. van Leer, *SIAM Rev.* **25**, 35 (1983).
17. A. Harten and S. Osher, *SIAM J. Numer. Anal.* **24**, 279 (1987).
18. K. Holing, Ph.D. thesis, Norges Tekniske Høgskole, Trondheim, 1990.
19. T. J. R. Hughes and J. E. Marsden, *J. Elasticity* **8**, 97 (1978).
20. P. D. Lax, *Commun. Pure Appl. Math.* **10**, 537 (1957).
21. P. D. Lax, *Hyperbolic Systems of Conservation Laws and the Mathematical Theory of Shock Waves, Regional Conference Series in Applied Mathematics*, Vol. 11 (SIAM, Philadelphia, 1973).
22. R. Löhner, K. Morgan, J. Peraire, and M. Vahdati, *Int. J. Numer. Methods Fluids* **7**, 1093 (1987).
23. J. Mandel, *J. Mec.* **1**, 3 (1962).
24. V. V. Rusanov, *J. Comput. Math. Math. Phys. USSR* **1**, 267 (1961).
25. I. S. Sandler and D. Rubin, *Int. J. Num. Anal. Methods Geom.* **3**, 173 (1979).
26. C.-W. Shu and S. Osher, *J. Comput. Phys.* **83**, 32 (1989).
27. J. A. Trangenstein, *Proceedings, Workshop on Viscous and Numerical Approximation of Shock Waves, 1990*, to appear.
28. J. A. Trangenstein, *Impact Comput. Sci. Eng.* **2**, 1 (1990).
29. J. A. Trangenstein and P. Colella, *Commun. Pure Appl. Math.* **44**, 41 (1991).
30. J. A. Trangenstein and R. B. Pember, *SIAM J. Sci. Stat. Comput.* **12**, 180 (1991).
31. B. van Leer, *J. Comput. Phys.* **32**, 101 (1979).
32. H. C. Yee, in *Proceedings of the Seminar on Computational Aerodynamics, University of California*, Davis, edited by M. Hafez (AIAA, Washington, DC, 1986).
33. J. A. Zukas, T. Nicholas, H. F. Swift, L. B. Greszczuk, and D. R. Curran, *Impact Dynamics* (Wiley-Interscience, New York, 1982).